Supporting Information: Ruddlesden-Popper chalcogenides push the limit of mechanical stiffness and glass-like thermal conductivity in single crystals

Md Shafkat Bin Hoque, Eric R. Hoglund, Boyang Zhao, De-Liang Bao, Hao Zhou, Sandip Thakur, Eric Osei-Agyemang, Khalid Hattar, Ethan A. Scott, Mythili Surendran, John A. Tomko, John T. Gaskins, Kiumars Aryana, Sara Makarem, Adie Alwen, Andrea M. Hodge, Ganesh Balasubramanian, Ashutosh Giri, Tianli Feng, Jordan A. Hachtel, Jayakanth Ravichandran, Sokrates T. Pantelides, and Patrick E. Hopkins

Md Shafkat Bin Hoque, John A. Tomko, Kiumars Aryana
Department of Mechanical and Aerospace Engineering, University of Virginia, Charlottesville, Virginia 22904, USA

Eric R. Hoglund
Department of Materials Science and Engineering, University of Virginia, Charlottesville, Virginia 22904, USA
Center for Nanophase Materials Sciences, Oak Ridge National Laboratory, Oak Ridge, Tennessee 37830, USA

Boyang Zhao, Mythili Surendran, Adie Alwen, Andrea M. Hodge
Mork Family Department of Chemical Engineering and Materials Science, University of Southern California, Los Angeles, California 90089, USA

De-Liang Bao
Department of Physics and Astronomy, Vanderbilt University, Nashville, Tennessee 37235, USA

Hao Zhou, Tianli Feng
Department of Mechanical Engineering, University of Utah, Salt Lake City, Utah 84112, USA

Sandip Thakur, Ashutosh Giri
Department of Mechanical, Industrial, and Systems Engineering, University of Rhode Island, Kingston, Rhode Island 02881, USA

Eric Osei-Agyemang
Department of Materials Design and Innovation, University at Buffalo, The State University of New York, Buffalo, New York 14260, USA

Khalid Hattar
Nuclear Engineering, University of Tennessee, Knoxville, Tennessee 37996, USA
Sandia National Laboratories, Albuquerque, New Mexico 87185, USA

Ethan A. Scott
Department of Mechanical and Aerospace Engineering, University of Virginia, Charlottesville, Virginia 22904, USA
Sandia National Laboratories, Albuquerque, New Mexico 87185, USA

John T. Gaskins
Laser thermal analysis, Charlottesville, Virginia 22902, USA

Sara Makarem
Department of Materials Science and Engineering, University of Virginia, Charlottesville, Virginia 22904, USA

Ganesh Balasubramanian
Department of Mechanical and Industrial Engineering, University of New Haven, West Haven, Connecticut 06516, USA

Jordan A. Hachtel
Center for Nanophase Materials Sciences, Oak Ridge National Laboratory, Oak Ridge, Tennessee 37830, USA

Jayakanth Ravichandran
Mork Family Department of Chemical Engineering and Materials Science, University of Southern California, Los Angeles, California 90089, USA
Core Center for Excellence in Nano Imaging, University of Southern California, Los Angeles, CA, USA
Ming Hsieh Department of Electrical and Computer Engineering, University of Southern California, Los Angeles, CA, USA
Email: j.ravichandran@usc.edu

Sokrates T. Pantelides
Department of Physics and Astronomy, Vanderbilt University, Nashville, Tennessee 37235, USA
Department of Electrical and Computer Engineering, Vanderbilt University, Nashville, Tennessee 37235, USA
Email: pantelides@vanderbilt.edu

Patrick E. Hopkins
Department of Mechanical and Aerospace Engineering, University of Virginia, Charlottesville, Virginia 22904, USA
Department of Materials Science and Engineering, University of Virginia, Charlottesville, Virginia 22904, USA
Department of Physics, University of Virginia, Charlottesville, Virginia 22904, USA
Email: phopkins@virginia.edu

Md Shafkat Bin Hoque, Eric R. Hoglund, and Boyang Zhao contributed equally to this work.

Jayakanth Ravichandran, Sokrates T. Pantelides, and Patrick E. Hopkins are corresponding authors.

S1. Growth and characterization details of $BaZrS_3$ and its RP derivatives

The $BaZrS_3$ and $Ba_3Zr_2S_7$ single crystals are synthesized using the flux method, details of which can be found in previous publications.[1] 1 g of $BaCl_2$ powder (Alfa Aesar, 99.998%) is grounded and mixed with 0.5 g of stoichiometric mixtures of precursor powders (BaS, Zr, and S), and loaded into a quartz tube. For $BaZrS_3$, the tube is heated to 1050 °C at a rate of 1.6 °C/min, held at 1050 °C for 100 h, cooled to 800 °C at a rate of 0.1 °C/min, and then to room temperature in an uncontrolled manner by shutting off the furnace. For $Ba_4Zr_3S_{10}$, the tube is heated to 1050 °C at a rate of 0.3 °C/min, held at 1050 °C for 40 h, cooled to 400 °C at a rate of 1 °C/min, and then to room temperature in an uncontrolled manner. $Ba_4Zr_3S_{10}$ is formed as a secondary phase twined with some large $Ba_3Zr_2S_7$ crystals. X-ray diffraction along 001 orientation[2] is used to characterize their existence, so $Ba_4Zr_3S_{10}$ layers are exfoliated to access them. The obtained samples are washed repeatedly with deionized water and isopropyl alcohol to remove excess flux before drying in airflow. The crystal dimensions are on the order of $\sim$100 μm. Amorphous $BaZrS_3$ thin films are grown from a phase pure $BaZrS_3$ target in a background gas mixture of hydrogen sulfide and argon (Ar-H_2S) on $LaAlO_3$ substrate. The dense, polycrystalline target is prepared by sintering $BaZrS_3$ powders by high pressure torsion method.[3]

X-ray diffraction (XRD) is used to investigate the crystal structures. Twining is commonly observed across large crystals of dozens to hundreds of micrometers scale: $BaZrS_3$ is twined along all three orthorhombic orientations which resembles a cubic diffraction structure but reveals the orthorhombic structures. As we segregate the twinning domains, $Ba_4Zr_3S_{10}$ is commonly uniaxially twined with $Ba_3Zr_2S_7$ that can be later exfoliated to get pure $Ba_3Zr_2S_7$ and $Ba_4Zr_3S_{10}$.

After segregating the twinning domains by cutting the crystals smaller, we observe consistent crystal structures in $BaZrS_3$ and $Ba_3Zr_2S_7$ as previously reported in Niu *et al.*;[2] with very low level of extended defects such as cracks and high-angle grain boundaries, also reported in Zhao *et al.*[4] and Chen *et al.*[5] These results reveal high crystal quality across several-micrometer scales, which are larger than the heat dissipation profiles in TDTR.

S2. Time-domain thermoreflectance (TDTR)

Figure S1(a) shows the best-fit thermal model to the TDTR data for the $BaZrS_3$, $Ba_3Zr_2S_7$, and $Ba_4Zr_3S_{10}$ single crystals. For all the measurements, the pump and probe beams are coaxially focused to $\sim$20 and 11 μm $1/e^2$ diameters, respectively on the sample surface. Prior to the measurements, all the samples are coated with an $\sim$80 nm aluminum film via electron beam evaporation for optothermal transduction.[6] Our TDTR setup is calibrated with a sapphire and a high purity fused silica wafer.

In TDTR, we fit for the thermal conductivity of the specimen and thermal boundary conductance between the aluminum transducer and specimen. Figure S1(b) shows the TDTR sensitivity calculations for the $BaZrS_3$ crystal. The sensitivity analysis is performed following the methodology published in prior literature.[7–9] As exhibited here, TDTR measurements have low sensitivity to the thermal boundary conductance and high sensitivity to the $BaZrS_3$ thermal conductivity. TDTR measurements also have high sensitivity to the volumetric heat capacity of the aluminum transducer and $BaZrS_3$ crystals.

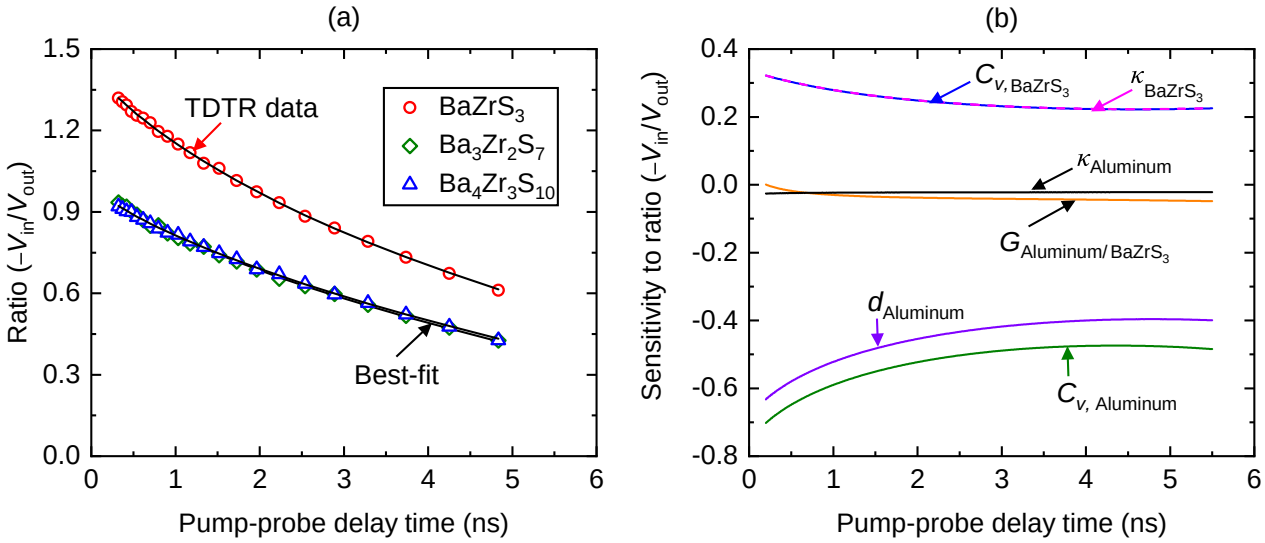

Figure S1: (a) Best-fit thermal model to the TDTR data for $BaZrS_3$, $Ba_3Zr_2S_7$, and $Ba_4Zr_3S_{10}$ crystals at room temperature. (b) Sensitivity of TDTR measurements to the ratio of in-phase to out-of-phase signal ($-V_{in}/V_{out}$) for $BaZrS_3$ at room temperature. Here, C_v, κ, G, and d represent volumetric heat capacity, thermal conductivity, thermal boundary conductance, and thickness, respectively.

S3. Steady-state temperature rise during TDTR measurements

Since the RP phases possess ultralow thermal conductivity, steady-state temperature rise from pulsed laser heating can be a major concern, particularly at low temperatures. Therefore, at each temperature, we calculate the steady-state temperature rise for the precise aluminum/sample geometry from the numerical solution to the cylindrical heat equation.[10] For each sample, we optimize the laser power to obtain good signal to noise ratio and minimal steady-state temperature rise. The maximum steady-state temperature rise observed in our study is 11 K. This degree of steady-state temperature rise is not expected to change the properties of aluminum and samples significantly to cause any error.[11]

S4. Uncertainty analysis

We calculate the uncertainty ($\triangle$) of TDTR measurements using the following equation[12–14]

$$\triangle = \sqrt{(\sigma)^2 + \left(R \cdot \frac{\delta_\phi}{S_\kappa}\right)^2 + \sum \left(\frac{S_\alpha}{S_\kappa} \cdot \frac{\delta_\alpha}{\alpha}\right)^2} \tag{S1}$$

here the first term σ represents the standard deviation of multiple measurements across different spots. The second term $R\frac{\delta_\phi}{S_\kappa}$ represents the uncertainty in determining the absolute value of the phase from the lock-in amplifier. R, δ_ϕ, and S_κ stand for the ratio of in-phase to out-of-phase signal, uncertainty of the phase, and sensitivity of R to κ in the thermal model, respectively. The third term $\frac{S_\alpha}{S_\kappa}\frac{\delta_\alpha}{\alpha}$ represents the propagation of uncertainty from individual input parameters to the thermal model. δ_α and S_α are uncertainty of parameter α and sensitivity of R to α in the thermal model, respectively.

We conduct the TDTR measurements at 8.4 MHz modulation frequency. At such high modulation frequency, the signal noise and δ_ϕ is quite small.[7] Therefore, the main sources of uncertainty in the

TDTR measurements are the standard deviation and input parameters.

The four input parameters to the thermal model are: volumetric heat capacity of aluminum and samples, aluminum transducer thickness, and aluminum thermal conductivity. The volumetric heat capacities of aluminum and samples are adopted from literature [15] and density functional theory (DFT) calculations, respectively. The thickness and thermal conductivity of the aluminum transducer are measured by picosecond acoustics [16] and four-point probe using the Wiedemann–Franz law [17], respectively.

Figure S2(a)-(d) shows the contour uncertainty analysis for various input parameters. The dashed lines represent the 95% confidence interval for the thermal conductivity corresponding to a specific value of the input parameter. This confidence interval confirms the uncertainty bounds of thermal conductivity for the parameters. Details of the contour uncertainty analysis can be found in previous publications. [18]

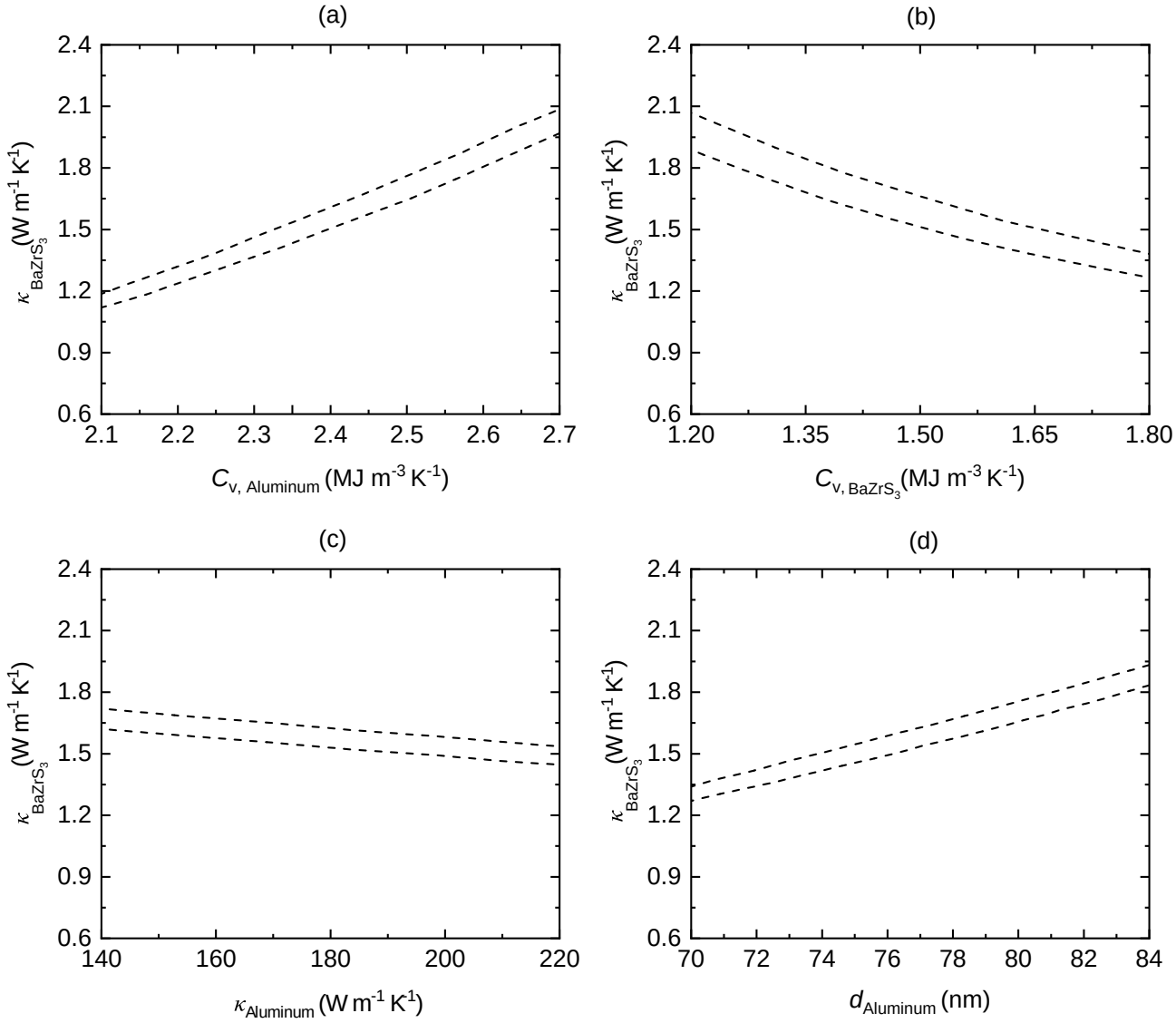

Figure S2: Uncertainty contour analysis of TDTR measurements showing a combination of $BaZrS_3$ thermal conductivity and (a) volumetric heat capacity of aluminum (2.42 MJ m^{-3} K^{-1}), (b) volumetric heat capacity of $BaZrS_3$ (1.505 MJ m^{-3} K^{-1}), (c) aluminum thermal conductivity (180 W m^{-1} K^{-1}), and (d) aluminum thickness (77 nm).

S5. Steady-state thermoreflectance (SSTR)

Along with TDTR, we employ another optical pump-probe technique named steady-state thermoreflectance (SSTR) to measure the thermal conductivity. Unlike TDTR, SSTR technique is insensitive to the volumetric heat capacity of aluminum and samples. We employ this technique to validate the volumetric heat capacity assumed for amorphous $BaZrS_3$ film. In SSTR setup, a continuous wave pump laser (532 nm wavelength) is modulated at 100 Hz frequency to create steady-state temperature rise at the sample surface. The reflectivity change and temperature rise are detected by a continuous wave probe laser (786 nm wavelength). By changing the pump laser power, the heat flux deposited on the sample surface and corresponding steady-state temperature rise can be changed. By correlating the pump laser power and temperature rise via Fourier's law, the thermal conductivity of any material can be derived. More details regarding the SSTR setup can be found in previous publications.[12,19,20] We use $1/e^2$ pump and probe diameters of $\sim$20 μm for the measurements.

S6. In-plane thermal conductivity measurements of $Ba_3Zr_2S_7$

We use TDTR technique to first measure the thermal conductivity of $Ba_3Zr_2S_7$ crystals along the *c*-axis. The measured value is presented as the cross-plane thermal conductivity (i.e., 0.45 ± 0.07 W m^{-1} K^{-1}).

We next tilt the crystals by 90° and measure the thermal conductivity perpendicular to the *c*-axis. This value is presented as the in-plane thermal conductivity (i.e., 1.06 ± 0.14 W m^{-1} K^{-1}).

Figure S3 provides visual illustrations of in-plane and cross-plane thermal conductivity measurements by TDTR. Since we are physically tilting the crystals by 90°, we can use the same modulation frequency and spot sizes for the measurements without impacting sensitivity.

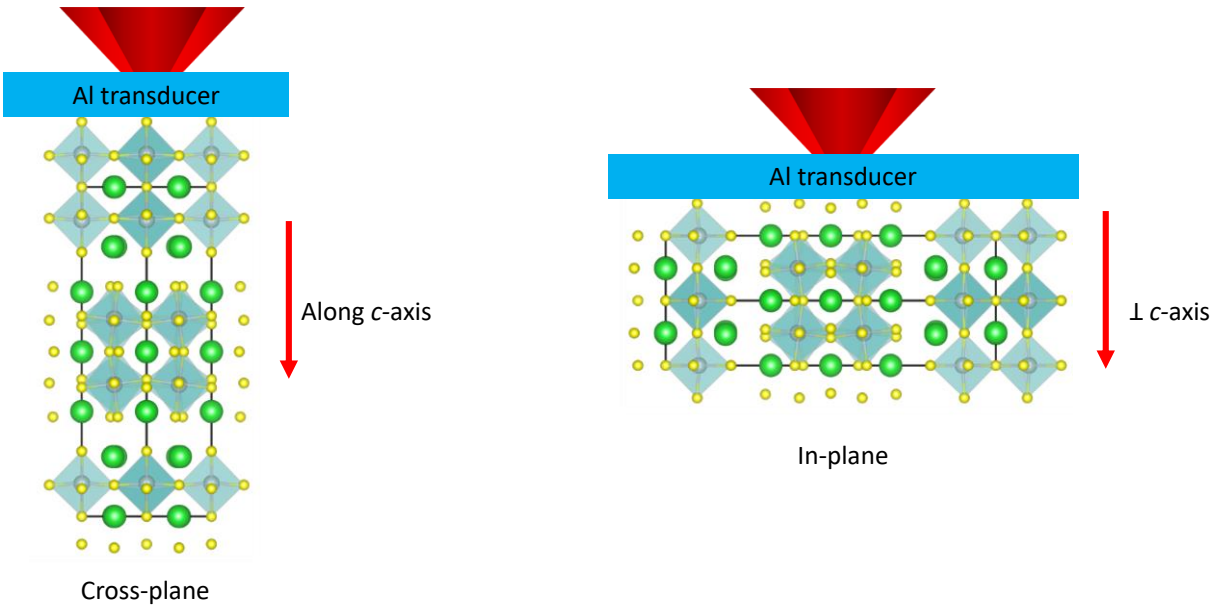

Figure S3: Cross-plane and in-plane thermal conductivity measurements by tilting the $Ba_3Zr_2S_7$ crystals.

Figure S4 shows the TDTR sensitivity calculations for $Ba_3Zr_2S_7$ thermal conductivity measurements ($\perp$ c-axis). As shown here, TDTR measurements are highly sensitive to the transducer thickness, which we determine using picosecond acoustics. The details of TDTR uncertainty analysis are discussed in section S4.

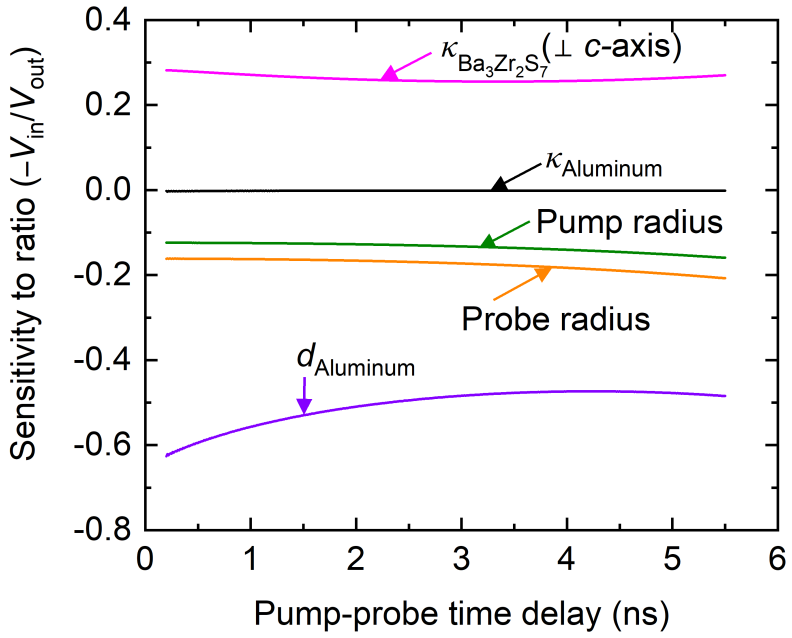

Figure S4: Sensitivity of TDTR measurements to the ratio of in-phase to out-of-phase signal ($-V_{in}/V_{out}$) for $Ba_3Zr_2S_7$ ($\perp$ c-axis).

S7. Volumetric heat capacity of $BaZrS_3$, $Ba_3Zr_2S_7$, and $Ba_4Zr_3S_{10}$

The volumetric heat capacity of crystalline $BaZrS_3$ and $Ba_3Zr_2S_7$ are calculated using DFT. Within the framework of DFT, the projector augmented wave method (PAW)[21] as implemented in the Vienna ab initio simulation package (VASP)[22] code is employed for relaxing the cell parameter and atomic positions of all perovskite unit cells. The PBEsol[23] functional for solids is utilized for relaxing the unit cell and atomic positions. The Methfessel-Paxton[24] smearing scheme with the gamma parameter is set to 0.1 eV and an energy cut-off of 500 eV is used for the planewaves expansion. A $5 \times 5 \times 1$ Monkhorst-Pack[25] special grid sampling of the k-points is used for integration in the Brillouin zone for structural optimization. For resolution of the Kohn-Sham equations, the self-consistent field procedure is considered by setting energy changes for each cycle at 10^{-5} eV as the convergence criterion between two successive iterations. The atomic forces are calculated by minimizing the total forces until the energy convergence is less than 10^{-3} eV. The interatomic force constants (IFCs) are computed by utilizing density functional perturbation theory with a $2 \times 2 \times 1$ supercell including up to the seventh nearest neighbor interactions. The PHONOPY[26] code is used to obtain the harmonic displacements while considering all neighboring interactions. For the anharmonic interactions, a $2 \times 2 \times 1$ supercell with up to the seventh neighbor interactions is employed with the THIRDORDER.PY code.[27,28]

Figure S5 shows the volumetric heat capacity of crystalline $BaZrS_3$ and $Ba_3Zr_2S_7$. We assume that the crystalline and amorphous $BaZrS_3$ possess the same volumetric heat capacity. To ensure the validity of this assumption, we measure the room-temperature thermal conductivity of a $\sim$107 nm amorphous $BaZrS_3$ film grown on silicon substrate via both TDTR and SSTR techniques. The TDTR technique is sensitive to heat capacity whereas the SSTR is insensitive to it. The measured thermal conductivity is in excellent agreement between the two techniques, thus proving the accuracy of the volumetric heat capacity assumed for amorphous $BaZrS_3$ in TDTR. We further assume that the $Ba_3Zr_2S_7$ and $Ba_4Zr_3S_{10}$ possess the same volumetric heat capacity. A 10% uncertainty is used with all the heat capacity values in TDTR measurements.

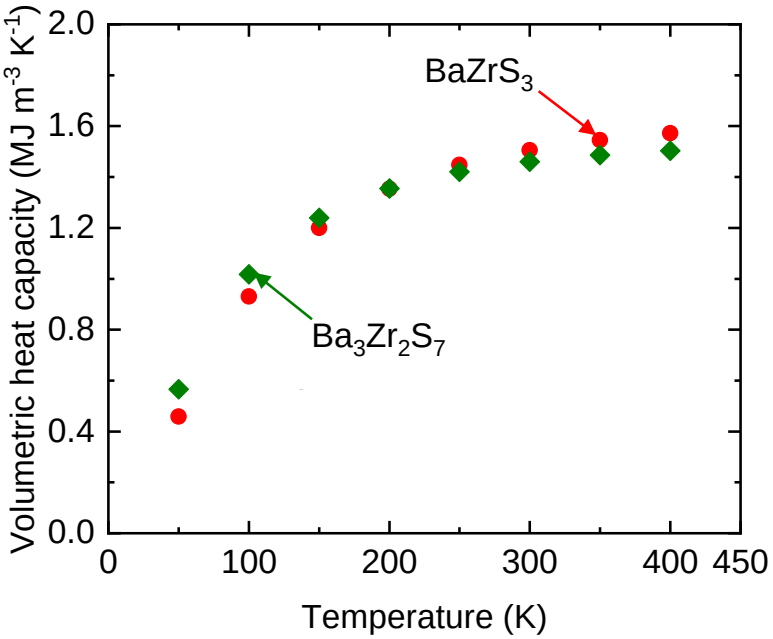

Figure S5: Volumetric heat capacity of crystalline $BaZrS_3$ and $Ba_3Zr_2S_7$ calculated via DFT.

S8. Ion irradiation of the $BaZrS_3$ and $Ba_4Zr_3S_{10}$ crystals

For the irradiation, six crystals of each material are carbon-taped onto a silicon substrate and loaded into the implant chamber. Afterwards, the chamber is pumped down to a pressure on the order of 10^{-7} torr. Due to the small size of the crystals ($\sim$100 $\times$ 100 $\times$ 100 μm^3) relative to the incident ion beam, spatial uniformity is achieved during the implantation. Nominal fluences ranging from 1.6 $\times$ 10^{11} to 8 $\times$ 10^{13} cm^{-2} are applied to each material.

TEM images of irradiated $Ba_4Zr_3S_{10}$ crystals are shown in Figure S6. As exhibited here, when the ion dose is 1.6 $\times$ 10^{11} cm^{-2}, no visible damage is observed in the crystal. However, as the ion dose is increased to 4.8 $\times$ 10^{13} cm^{-2}, amorphous pockets are introduced in the system. For both ion doses, the layerings of $Ba_4Zr_3S_{10}$ remain uninterrupted. This verifies the strong bonding across the rock-salt layers in the RP phases and makes them suitable for deep space applications in radiation environments.

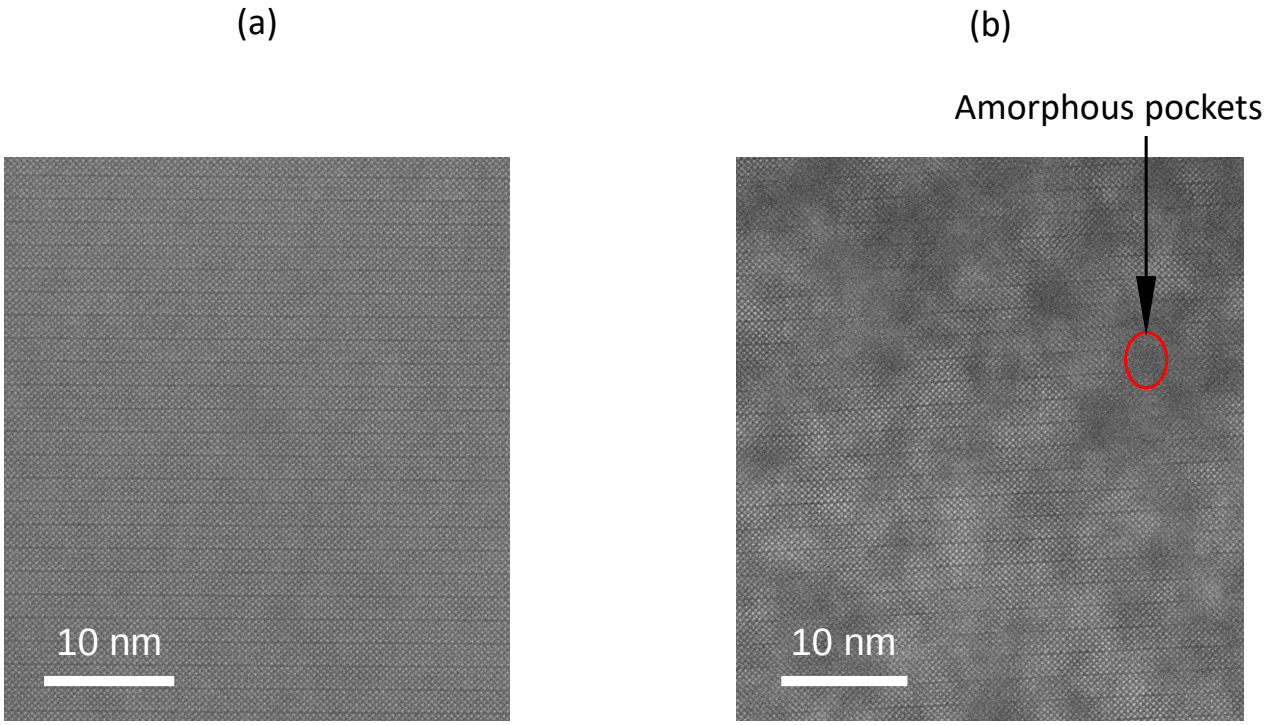

Figure S6: TEM images of $Ba_4Zr_3S_{10}$ crystals corresponding to (a) 1.6 $\times$ 10^{11} and (b) 4.8 $\times$ 10^{13} cm^{-2} ion doses.

S9. Presence of nano-domains in $BaZrS_3$ crystals

One of the biggest requirements for any thermoreflectance measurement is optically smooth sample surface. To obtain such surface quality, we mechanically polish the samples. Polishing deforms the crystals and creates nano-scale domains in $BaZrS_3$ as exhibited in Figure S7(a). The presence of such nano-domains can obfuscate the origin of thermal behaviors in $BaZrS_3$. Therefore, as an alternate to polishing, we use cleaving on several $BaZrS_3$ crystals. Although cleaving does not deform the material and create nano-domains, obtaining large quantities of optically smooth crystals can be highly challenging via cleaving. As a result, we use polished $BaZrS_3$ crystals for many of our measurements. The $BaZrS_3$ thermal conductivity shown in Figure 2(a) corresponds to a cleaved crystal, whereas the ones shown in Figure 2(c) belong to polished crystals. The cleaved and polished $BaZrS_3$ crystals have thermal conductivities of 1.55 ± 0.2 and 1.21 ± 0.18 W m^{-1} K^{-1}, respectively, at room temperature.

Polishing also deforms the RP crystals and creates domains. However, due to the high stiffness of the RP phases, the domain sizes are greater than 500 nm as shown in Figure S7(b). At such length scales, the domains are not expected to impact the thermal conductivity of the RP phases.[29] As a result, we use mechanically polished RP crystals for all of our measurements.

The thermal conductivity of the cleaved and polished $BaZrS_3$ crystals are shown in Figure S7(c) as a function of temperature. Due to phonon scattering at the domain boundary, the thermal conductivity of the polished crystal is lower than the cleaved one throughout the temperature range.

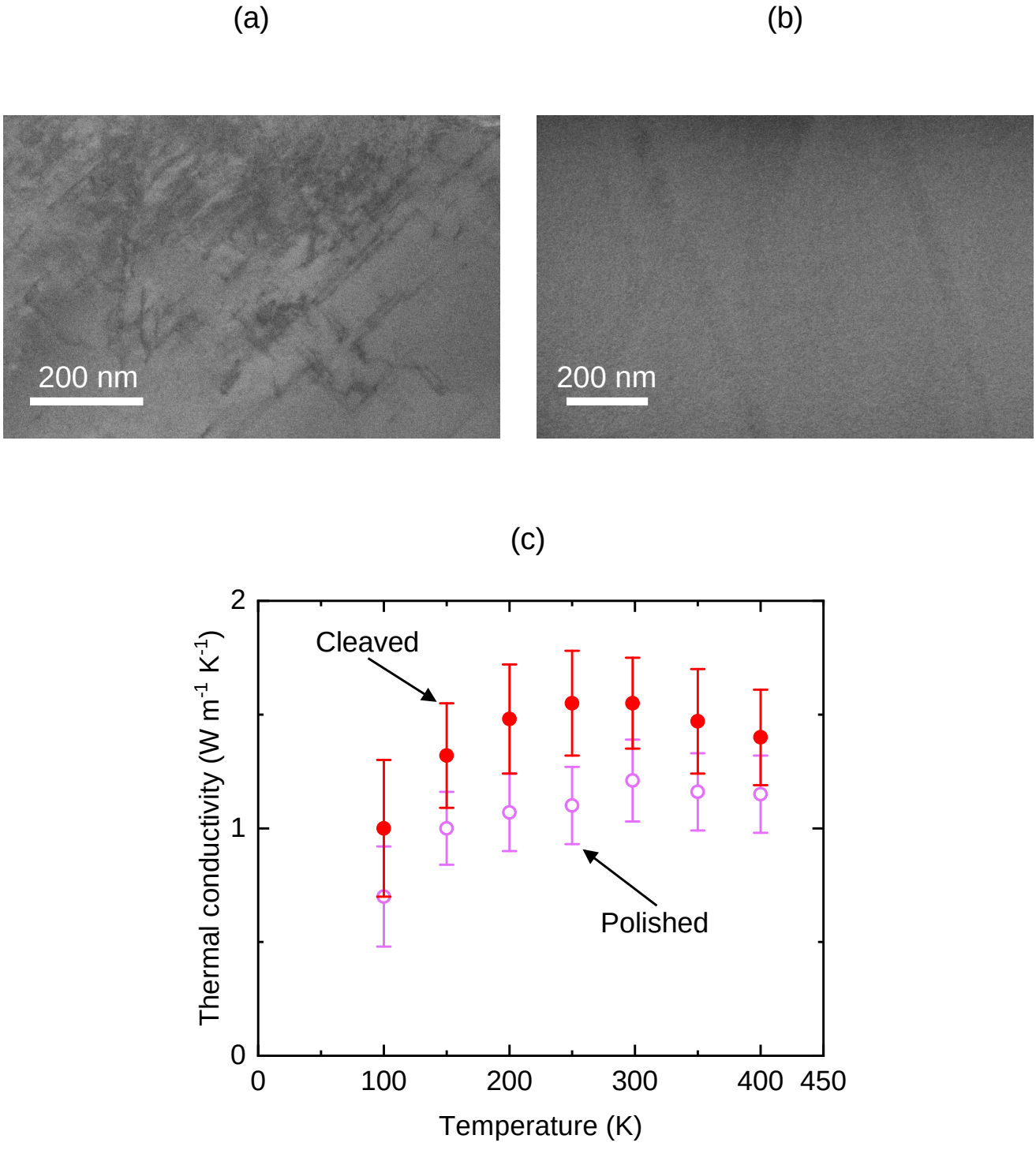

Figure S7: TEM images of domains in (a) $BaZrS_3$ and (b) $Ba_3Zr_2S_7$ crystals. (c) Thermal conductivity of cleaved and polished $BaZrS_3$ crystals as a function of temperature.

S10. Machine learning molecular dynamics (MLMD) simulation details

To construct the training database of machine learning potential, first principles calculations of both $BaZrS_3$ and $Ba_3Zr_2S_7$ are performed by using VASP[30] with the PAW[31] method based on the DFT. Local density approximation (LDA)[32] is chosen as the exchange-correlation functional. The plane-wave energy cutoff is selected as 500 eV. The primitive cell is first relaxed with the energy convergence threshold of 10^{-8} eV and the force convergence threshold of 10^{-4} eV/Å between atoms. For $BaZrS_3$, the calculational primitive cell contains 20 atoms following the *Pnmb* symmetry, where the lattice constants are 7.03 Å, 9.86 Å, and 6.89 Å along *a*, *b*, and *c* directions, respectively. The **k**-mesh is set to 7 × 5 × 7. For $Ba_3Zr_2S_7$, the calculational primitive cell contains 24 atoms following the *I4mmm* symmetry, where the lattice constants are 4.92 Å, 4.92 Å, and 25.24 Å along *a*, *b*, and *c* directions, respectively. The **k**-mesh is set to 10 × 10 × 2. After the relaxation, the VASP + PHONOPY combination is utilized to calculate the phonon properties of $BaZrS_3$ and $Ba_3Zr_2S_7$. *Ab initio* molecular dynamics (AIMD) simulations are performed to sample the potential energy surface. For $BaZrS_3$ and $Ba_3Zr_2S_7$, 2 × 2 × 2 supercells are adopted containing 160 and 192 atoms, respectively, in the simulation domains. The time step of AIMD is set to 5 fs and a total step of 8000 is run for each individual AIMD. Independent AIMDs at 100 K, 200 K, 300 K, 400 K, and 500 K with Canonical ensemble (NVT) are performed. During the AIMD process, energies, forces, and stresses are recorded together with corresponding atomic configurations to form the training database for machine learning potential.

The potential energy surface is approximated by moment tensor potential (MTP) trained by Machine-Learning Interatomic Potentials (MLIP) package.[33] MTP represents the energy of an atomic configuration cfg ($E^{\mathrm{mtp}}(\mathrm{cfg})$) as a sum of contributions of local atomic environments of each atom, denoted by n_i, shown as

$$E^{\mathrm{mtp}}(\mathrm{cfg}) = \sum_{i=1}^{n} V(n_i) \tag{S2}$$

MTP with different levels are provided and a higher level means more fitting parameters, potential higher accuracy and possible issues of overfitting. Given a training database containing K configurations cfg_k (k=1, 2, ..., K) with their corresponding DFT calculated energies, forces, and stresses, the training process of MTP is minimizing the following expression:

$$\sum_{k=1}^{K}\left[w_e\left(E^{\mathrm{mtp}}(\mathrm{cfg}_k)-E^{\mathrm{DFT}}(\mathrm{cfg}_k)\right)^2+w_f\sum_{k=1}^{N_k}\left(\mathrm{f}_i^{\mathrm{mtp}}(\mathrm{cfg}_k)-\mathrm{f}_i^{\mathrm{DFT}}(\mathrm{cfg}_k)\right)^2+w_s\left(\sigma^{\mathrm{mtp}}(\mathrm{cfg}_k)-\sigma^{\mathrm{DFT}}(\mathrm{cfg}_k)\right)^2\right]$$

where N_k is the number of atoms in the kth configuration, w_e, w_f, and w_s are non-negative weights. More details about MTP and the training process can be found in Novikov *et al.*[33] In this work, MTP with the level of 22 is adopted to fit the potential energy surface and the training step is set to be 20,000.

Once the MTP is developed, equilibrium molecular dynamics (EMD) is performed via LAMMPS[34] package to get the lattice thermal conductivity, κ. A supercell of 10 × 10 × 10 conventional cell is adopted for $BaZrS_3$ and 10 × 10 × 10 for $Ba_3Zr_2S_7$, respectively, which should be large enough to avoid size effect.[35] The time step of EMD is 5 fs, and periodic boundary conditions are implemented in all three directions. The simulation is carried out first by 2 ns NVT, followed by a 2 ns NVE to fully relax the lattice, and then another NVE of 4 ns, during which the heat current $\boldsymbol{J}$ is recorded. Based on the

Kubo-formula,[36,37] κ along a certain direction α is proportional to the integral of autocorrelation of heat current:

$$\kappa_\alpha = \frac{1}{k_B V T^2} \int_0^\infty (J_\alpha(0) \cdot J_\alpha(t)) dt \tag{S3}$$

where k_B is Boltzmann constant, V is the volume of the simulation domain, T is temperature, and t is time. In LAMMPS, the heat current vector $\boldsymbol{J}$ is defined as

$$\boldsymbol{J} = \sum_i v_i E_i - \sum_i \boldsymbol{S}_i v_i = \sum_i v_i E_i + \sum_{i<j} (\boldsymbol{F}_{ij} \cdot v_i) \boldsymbol{r}_{ij} \tag{S4}$$

where E_i is the total energy of the ith atom, v_i is the velocity vector of the ith atom, $\boldsymbol{F}_{ij}$ is the force interaction between the ith and jth atom, and $\boldsymbol{r}_{ij}$ represents the position vector between the ith and jth atom. The final κ is averaged over 8 independent EMD simulations at each temperature with different initial velocities. Quantum correction is taken into account due to the classical specific heat used in LAMMPS is much higher than the real specific heat at low temperature.[38]

S11. Spectral energy density (SED) calculations

To gain insights into the intrinsic mechanisms that dictate the thermal transport in $BaZrS_3$ and its RP phase $Ba_3Zr_2S_7$ structures, we calculate the phonon mode specific properties by performing spectral energy density (SED) calculations in MD simulations, which is given as[39,40]

$$\Phi(\mathbf{q},\omega) = \frac{1}{4\pi\tau N_T} \sum_\alpha^3 \sum_b^B m_b \left| \int_0^\tau \sum_{n_{x,y,z}}^{N_T} \dot{u}_\alpha \begin{pmatrix} n_{x,y,z} \\ b \end{pmatrix}; t \right) \times exp\left[i\mathbf{q} \cdot \mathbf{r} \begin{pmatrix} n_{x,y,z} \\ 0 \end{pmatrix} - i\omega t \right] dt \Bigg|^2 \tag{S5}$$

where τ is the total simulation time, α is the cartesian direction, $n_{x,y,z}$ is a unit cell, N_T is the number of unit cells in the crystal, b is the atom label in a given unit cell, B is the atomic number in the unit cell, m_b is the mass of atom b in the unit cell, $\dot{u}_\alpha$ denotes the velocity along the α direction at time t, and $\mathbf{r}$ is the equilibrium position of each unit cell.

To ensure a high resolution in our SED calculations, we create the computational domain for both $BaZrS_3$ and its RP phase $Ba_3Zr_2S_7$ structures with $N_T = 400$ (representing the total number of unit cells) and perform SED calculations for 100 $\mathbf{q}$-points. Initially, we equilibriate our supercell structure using the Nosé-Hoover thermostat and barostat[41] for 1 ns with a time step of 0.5 fs where the number of particles, pressure, and temperature of the system are held constant at ambient pressure. After the NPT integration, we further equilibriate our structures in the NVT ensemble, keeping the volume and temperature constant for an additional 1 ns. Finally, for the data collection for our SED calculations, we record the velocities and positions of each atom in the microcanonical ensemble (or NVE ensemble) for a total of 1.5 ns.

S12. Elastic modulus measurements and derivation of sound speed

We measure the elastic modulus of the $BaZrS_3$ crystals using a nanoindeter (MTS XP) based on the standard continuous stiffness measurement (CSM) method.[42] Before the measurements, the nanoindenter is calibrated with a silica standard. Details of the calibration procedure can be found in previous publications.[43,44] The elastic modulus of $BaZrS_3$ is determined to be 84.2 $\pm$ 5.4 GPa. This value is in agreement with literature.[45]

The elastic modulus of $Ba_3Zr_2S_7$ is measured by a Bruker Hysitron TI 950 Triboindenter. The indenter is calibrated with a single crystal quartz sample with known modulus and hardness (69.6 GPa and 9.25 GPa, respectively). The measured elastic modulus of $Ba_3Zr_2S_7$ is 69 $\pm$ 4.5 GPa. The indentation curves exhibit pop-in features, which are sudden displacement excursions; a common feature observed in single crystals.[46]

Assuming isotropic elastic properties, the sound speed components of $BaZrS_3$ can be derived using the following equations[47]

$$v_L = \sqrt{\frac{E(1-\nu)}{\rho(1+\nu)(1-2\nu)}} \tag{S6}$$

$$v_T = \sqrt{\frac{E}{2\rho(1+\nu)}} \tag{S7}$$

$$v_s = \frac{1}{3}(2v_T + v_L) \tag{S8}$$

where v_L, v_T, v_s, E, ρ, and ν represent longitudinal sound speed, transverse sound speed, sound velocity, elastic modulus, density, and Poisson's ratio, respectively. We take the density and Poisson's ratio to be 4.39 g cm^{-3} and 0.28 $\pm$ 0.05, respectively.[2] The derived sound speed components of $BaZrS_3$ are tabulated in Table S1. The error bars incorporate the uncertainty of the elastic modulus and Poisson's ratio.

To further verify the longitudinal sound speed, we use picosecond acoustics on a 416 nm crystalline $BaZrS_3$ film. Details of our picosecond acoustics metrology and data reduction can be found in previous publications.[47–49] Picosecond acoustics reveal the longitudinal sound speed of $BaZrS_3$ to be 4818 $\pm$ 512 m s^{-1}, in excellent agreement with the elastic modulus derived value. The error bar of the picosecond acoustic measurement incorporates the standard deviation and uncertainty of the film thickness ($\sim$44 nm).

Table S1: Longitudinal sound speed, transverse sound speed, and sound velocity of the $BaZrS_3$ crsytals.

Sound speed components	Velocity (m s^{-1})
v_L	4952 $\pm$ 410
v_T	2737 $\pm$ 112
v_s	3475 $\pm$ 143

S13. Elastic modulus calculations

To determine the stress-strain relationship for our $BaZrS_3$ and its RP phase $Ba_3Zr_2S_7$ structures, we use MLMD simulations to calculate the elastic moduli. We deform the simulation cell in the uniaxial direction using a strain rate of 10^8 s^{-1}. Concurrently, we maintain zero pressure at the boundaries in the remaining two lateral directions. This process is performed under the NPT ensemble, where the system's number of particles, pressure, and temperature are kept constant. The strain is computed at intervals of 0.5 fs using the formula $(L_x - L)/L$, where L_x represents the current length and L denotes the initial length of the domain in the direction of the applied strain. Simultaneously, the stress of the entire structure is recorded every 50 fs to enable the generation of a stress-strain relationship for the structures.

For $BaZrS_3$, we calculate a Young's modulus value of 85 GPa in the cross-plane direction. For $Ba_3Zr_2S_7$, we calculate Young's modulus values of 64.5 GPa and 64.3 GPa in the in-plane directions, and 81.3 GPa in the cross-plane direction.

S14. Minimum limit and diffuson limit

Cahill *et al.*'s minimum limit model states that the lower bound of thermal conductivity can be achieved when the phonon mean free path reduces to half of its wavelength.[50] This model assumes that the heat is transported through a solid via random walks between localized osciallators. Cahill *et al.*'s minimum limit model is also known as the amorphous limit model and can be expressed as the following[51]

$$\kappa_g = \left(\frac{\pi}{6}\right)^{1/3} k_B n^{2/3} \left[v_L \left(\frac{T}{\theta_L}\right)^2 \int_0^{(\theta_L/T)} \frac{x^3 e^x}{(e^x-1)^2} dx + 2 v_T \left(\frac{T}{\theta_T}\right)^2 \int_0^{(\theta_T/T)} \frac{x^3 e^x}{(e^x-1)^2} dx \right] \tag{S9}$$

$$\theta_L = v_L \left(\frac{h}{2\pi k_B}\right) (6\pi^2 n)^{1/3} \tag{S10}$$

$$\theta_T = v_T \left(\frac{h}{2\pi k_B}\right) (6\pi^2 n)^{1/3} \tag{S11}$$

where κ_g, k_B, n, h, θ, and T represent thermal conductivity prediction, Boltzmann constant, number density, Planck constant, Debye temperature, and temperature, respectively.

Cahill *et al.*'s model has successfully predicted the thermal conductivity of many disordered solids and amorphous materials. However, several recent studies have showed that the thermal conductivity of a few materials can fall below this limit.[52–55] Therefore, to better estimate the theoretical lower bound of thermal conductivity, Agne *et al.*[56] predicted a model based on the diffuson-mediated thermal transport. Agne *et al.*'s diffuson model assumes that the heat is transported through a material via diffusons (i.e., non-propagating, delocalized vibrational modes). According to this diffuson model, the thermal conductivity (κ_d) can be expressed as

$$\kappa_d = \frac{n^{-2/3} k_B}{2\pi^3 v_s^3} \left(\frac{2\pi k_B T}{h}\right)^4 \int_0^{0.95\frac{\theta_D}{T}} \frac{x^5 e^x}{(e^x-1)^2} dx \tag{S12}$$

$$\theta_D = \frac{h}{2\pi k_B} (6\pi^2 n)^{1/3} v_s \tag{S13}$$

The minimum limit and diffuson limit shown in Figure 2(a) correspond to $BaZrS_3$ and are calculated using the properties mentioned in supporting information section S12.

S15. Anisotropic minimum thermal conductivity limit

As RP structured crystals has certain anisotropy, we use the anisotropic thermal conductivity limit proposed by Chen and Dames[57] for $Ba_3Zr_2S_7$. According to this model, the minimum thermal conductivity along the cross-plane direction ($\kappa_{min-c,layered}$) of a layered material can be expressed as:

$$\kappa_{min-c,layered} = \sum_{pol} \frac{{k_B}^3}{6\pi(\frac{h}{2\pi})^2} \frac{v_c}{v_{ab}^2} \left[\int_0^{\frac{\theta_{D,c}}{T}} \frac{T^2 x^3 e^x}{(e^x-1)^2} dx + \frac{\theta_{D,c}^3}{T} \int_{\frac{\theta_{D,c}}{T}}^{\frac{\theta_{D,ab}}{T}} \frac{e^x}{(e^x-1)^2} \left(\frac{\theta_{D,ab}^2 - (Tx)^2}{\theta_{D,ab}^2 - \theta_{D,c}^2} \right)^{3/2} dx \right] \tag{S14}$$

Where k_B, h, θ_D, and T represent Boltzmann constant, Planck constant, c-axis sound velocity, ab-plane sound velocity, Debye temperature, and temperature, respectively.

For $Ba_3Zr_2S_7$, we derive $v_{c,L}$ and $v_{ab,L}$ (L represents longitudinal polarizations) from the elastic constants obtained via MD. The derived values are 4288 and 3807 m s^{-1}, respectively. Using these values, the anisotropic minimum thermal conductivity model of Figure S8 is obtained. As elastic constants have an uncertainty of $\sim$12% and we assume v_T= 0.6v_L,[55] the anisotropic model of Figure S8 has an uncertainty of $\sim$15%.

The anisotropic version of the minimum thermal conductivity model is still higher than the experimental values of $Ba_3Zr_2S_7$. This can be attributed to the comparable bond strength across the rock-salt layers and $(BaZrS_3)_n$ layers. As a result, the sound velocities are also comparable between c-axis and ab-plane. In other anisotropic materials, such as WSe_2, the bonding and sound velocities are very different between c-axis and ab-plane.[57]

Due to comparable sound velocities between c-axis and ab-plane, the predictions of anisotropic thermal conductivity model are close to the predictions of isotropic thermal conductivity model.

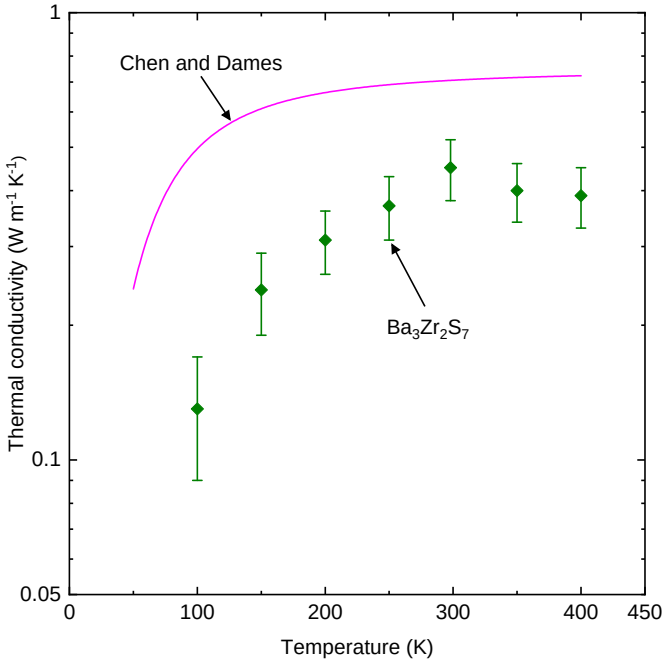

Figure S8: Anisotropic minimum thermal conductivity model[57] and experimental measurements of $Ba_3Zr_2S_7$.

S16. Machine learning potentials (MLPs)

In order to perform MLMD simulations over a wide temperature range, we develope two machine learning potentials (MLPs) for each of $BaZrS_3$ and $Ba_3Zr_2S_7$, respectively. One potential is for relatively low-temperature (LT) MLMDs and the other is for relatively high-temperature (HT) MLMDs. In particular, the LT-MLP of $BaZrS_3$ is used to run 100 K, 150 K, 200 K, and 250 K MLMDs, while the HT-MLP of $BaZrS_3$ is used to run 300 K, 350 K, and 400 K MLMDs. The LT-MLP of $Ba_3Zr_2S_7$ is for 100 K and 150 K MLMDs, while HT-MLP of $Ba_3Zr_2S_7$ is for 200 K, 250 K, 300 K, 350 K, and 400 K MLMDs.

Table S2: The root-mean-square (RMS) errors of energies per atom and atomic forces for MLPs across both the training and testing datasets.

RMS absolute difference	MLP ($BaZrS_3$)		MLP ($Ba_3Zr_2S_7$)	
	Train	Test	Train	Test
Energy per atom (meV)	0.348	0.354	0.293	0.311
Atomic force (eV/Å)	0.054	0.054	0.047	0.047

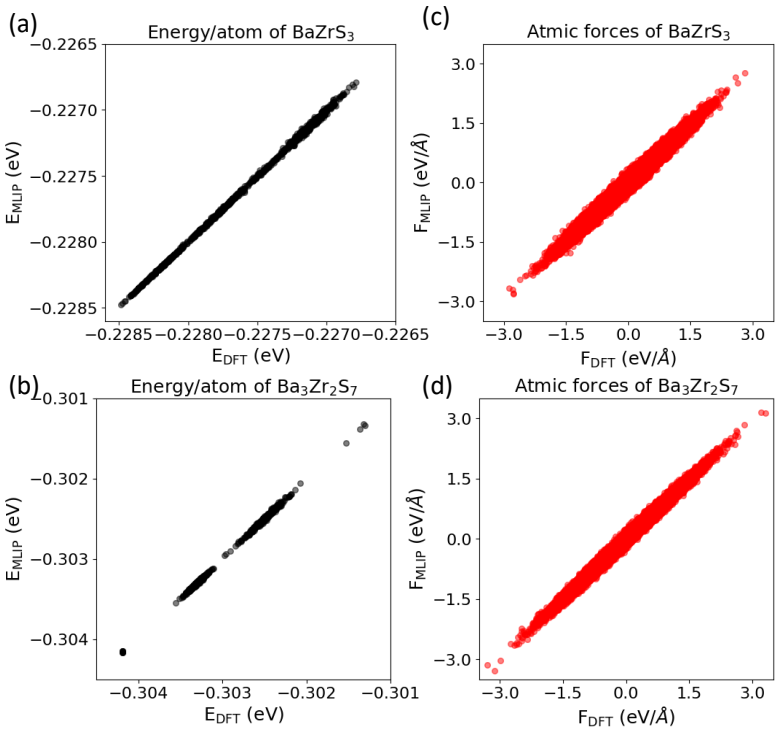

Figure S9: Discrepancies between the energy/atom and atomic forces obtained using the machine-learned force field (MLIP) and those obtained using DFT over the testing datasets for (a, c) $BaZrS_3$ and (b, d) $Ba_3Zr_2S_7$. The first and second coulums correspond to energy/atom and atomic forces, respectively

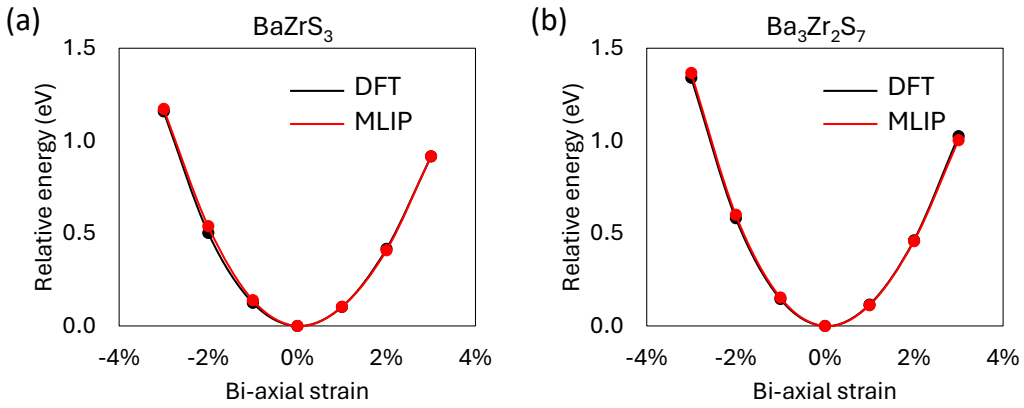

Figure S10: Calculated relative energies as a function of bi-axial strain between DFT and MLIP for (a) $BaZrS_3$ and (b) $Ba_3Zr_2S_7$. The results between DFT and MLIP show very good agreement.

S17. Literature data of elastic modulus/thermal conductivity (E/κ) ratio

The elastic modulus/thermal conductivity (E/κ) ratios of a wide range of single crystalline materials are listed in Table S3.

Table S3: The elastic modulus/thermal conductivity (E/κ) ratios of different groups of single crystalline materials at room temperature.

Group	Material	E (GPa)	E/κ (GPa m K W^{-1})
Superatom	Co_6S_8	4	18.18 [58]
	Co_6Se_8	2.3	12.78 [58]
	Co_6Te_8	0.62	4.77 [58]
	$[Co_6Se_8][C_{60}]_2$	8.1	32.4 [58]
	$[Co_6Te_8][C_{60}]_2$	1.5	9.38 [58]
Semiconductor	Diamond (I/ IIa/ IIb)	1144.81	1.27/0.49/0.84 [59–62]
	cBN	909	1.03 [63–65]
	AlN	374	1.17 [66,67]
	GaN	295	1.17 [68,69]
	Si	165.82	1.11 [59–62]
	Ge	135.4	2.25 [59–62]
	$AgSbTe_2$	49.49	72.78 [70,71]
	PbTe	67.23	28.01 [70,72]
	InAs	79.7	2.95 [73,74]
	PbSe	65.2	24.7 [75]
	PbS	70.2	25 [75]
Metal halide perovskite	$MAPbCl_3$ (cubic)	23	31.5 [76]
	$MAPbBr_3$ (cubic)	17.8	34.9 [76]
	$MAPbI_3$ (tetragonal)	12	35.3 [76]
	$CsPbBr_3$ (Orthorhombic)	13.5	29.35 [76]
	$FAPbBr_3$ (Orthorhombic)	10.2	20.82 [76]

Table S3: The elastic modulus/thermal conductivity (E/κ) ratios of different groups of single crystalline materials at room temperature (cont.).

Group	Material	E (GPa)	E/κ (GPa m K W^{-1})
Oxide	MgO	310	5.96[44,77]
	Al_2O_3	345	10.15[44]
	$SrTiO_3$	260.85	23.71[78–80]
	$BaZrO_3$	181	42.1[81]
	$La_2Zr_2O_7$	175	92.11[81]
	Y_2O_3-stabilized ZrO_2 (YSZ)	210	98.6[81]
	NiO	175	5.15[82,83]
	J14 ESO	152	51.53[44]
	J34 ESO	180.8	125.56[44]
	J36 ESO	229.9	143.69[44]
Layered materials	$Cs_3Bi_2I_6Cl_3$	17.4	87[84]
	$Cs_2PbI_2Cl_2$*	20.6	55.7[85]
	WSe_2	167.3	107.2[52,86]
	$(4N4)_2CuInCl_8$	9.9	38[87]
	$(4N4)_2CuRuCl_8$	9.7	32.3[87]
	$(3N)_4CuInCl_8$	5.9	21[87]
	$BaZrS_3$	84.2	54.3
	$Ba_3Zr_2S_7$	69	153.3

*$Cs_2PbI_2Cl_2$ is a RP material. The elastic modulus has been calculated from reported bulk modulus and shear modulus.

S18. Temperature-dependent thermal conductivity of perovskites

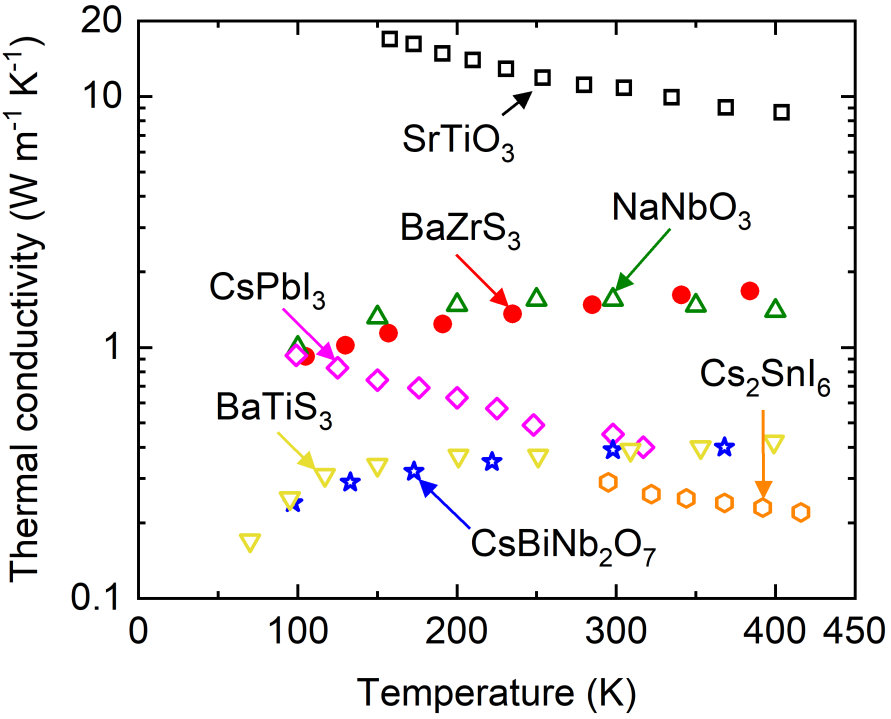

Figure S11: Temperature-dependent thermal conductivity of $BaZrS_3$, $SrTiO_3$,[88] $NaNbO_3$,[89] $CsPbI_3$,[90] Cs_2SnI_6,[91], $BaTiS_3$,[11] and $CsBiNb_2O_7$.[92] The solid and hollow symbols represent measurements taken in this study and the cited literature values, respectively.

S19. Phonon mean free path of $Ba_3Zr_2S_7$

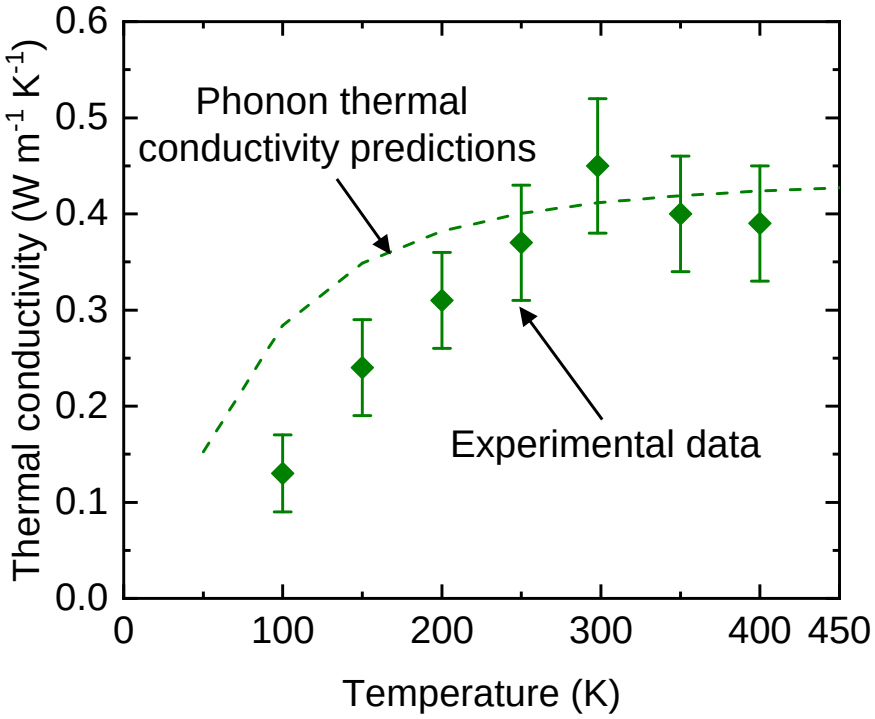

Figure S12: Comparison of phonon thermal conductivity assuming an average mean free path of 1 nm with experimental data.

S20. Heat-current autocorrelation functions

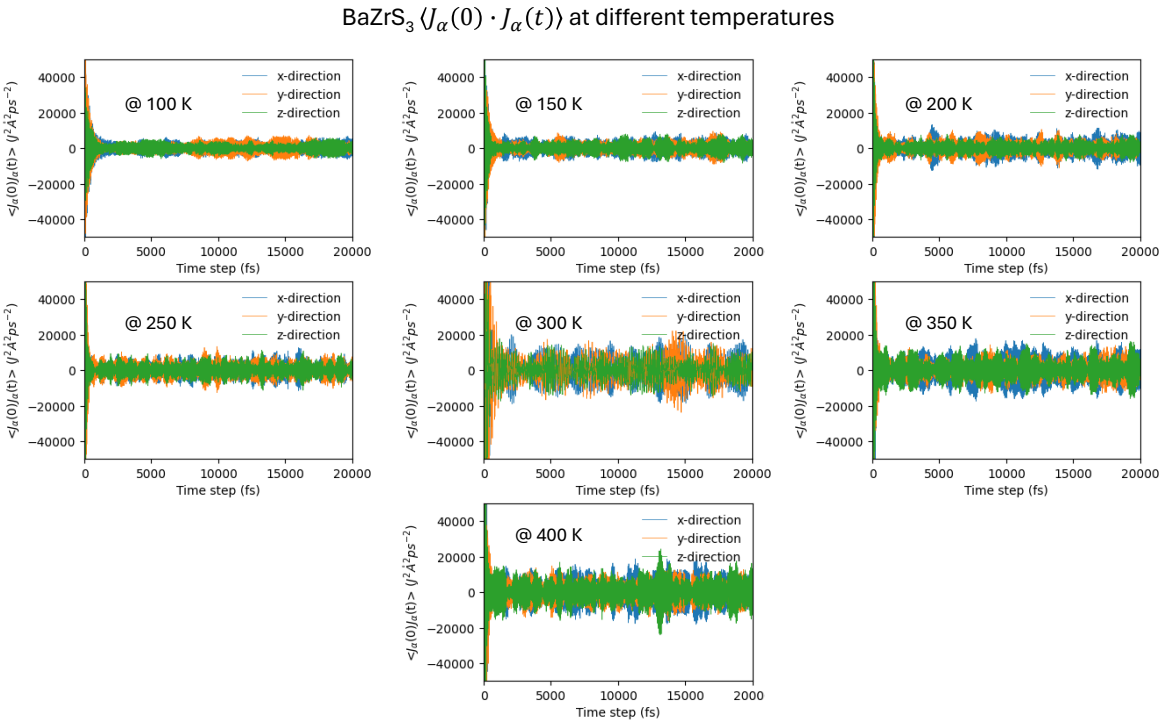

Figure S13: The calculated heat-current autocorrelation functions for $BaZrS_3$ at various considered temperatures. Recall that we performed eight independent MLMDs at each temperature. For simplicity, each panel in the figure represents one MLMD simulation case out of these eight independent cases. Blue, orange, and green colors represent x, y, and z-direction results, respectively.

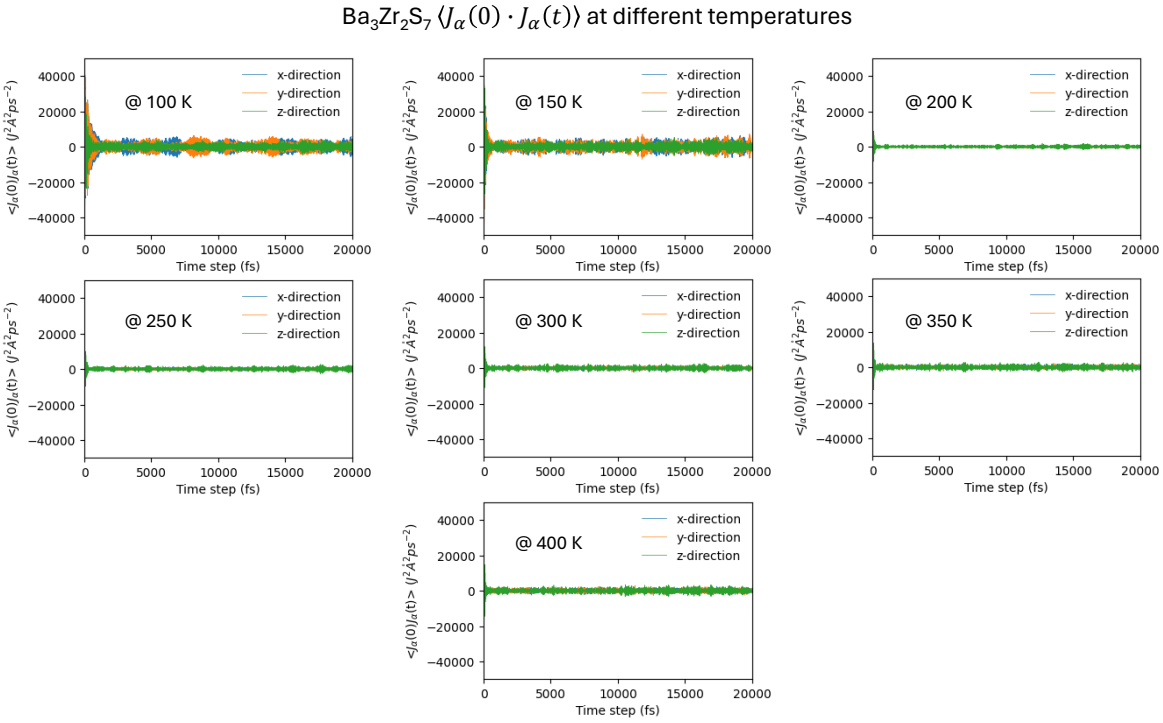

Figure S14: The calculated heat-current autocorrelation functions for $Ba_3Zr_2S_7$ at various considered temperatures. Recall that we performed eight independent MLMDs at each temperature. For simplicity, each panel in the figure represents one MLMD simulation case out of these eight independent cases. Blue, orange, and green colors represent x, y, and z-direction results, respectively.

S21. Calculated thermal conductivities vs correlation time

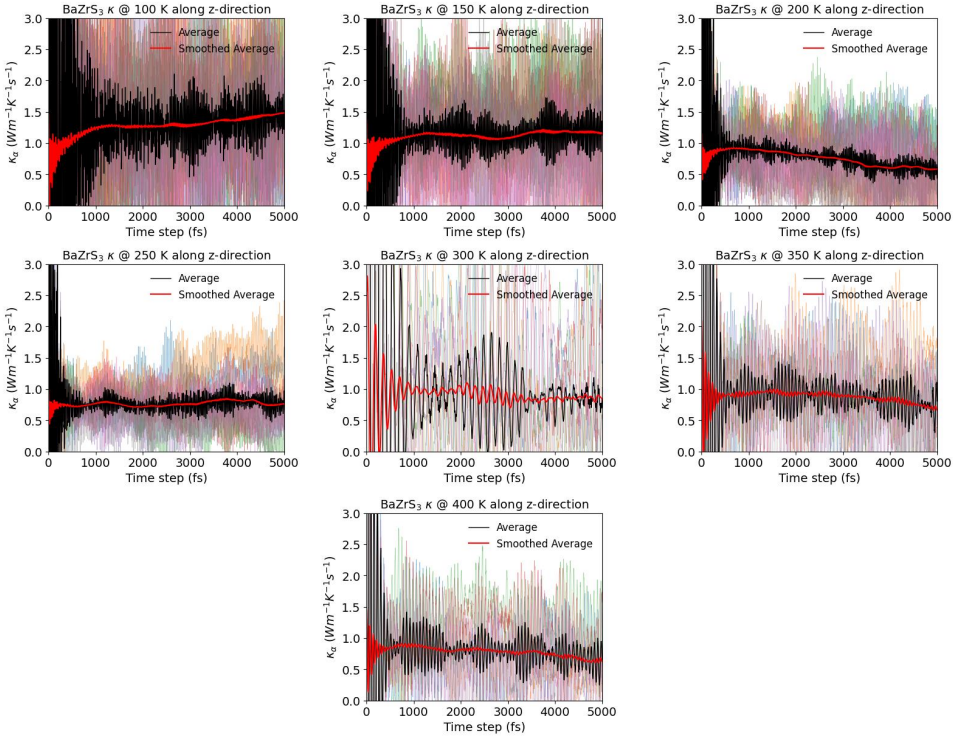

Figure S15: The calculated thermal conductivities of $BaZrS_3$ as a function of correlation time at various considered temperatures. Only the z-components of the thermal conductivity are plotted. Within each panel, the colorful curves represent the calculated results for all eight cases at each temperature. The black curves depict the average of the eight colorful curves, while the red curves are obtained by averaging every 200 data points from the black curve.

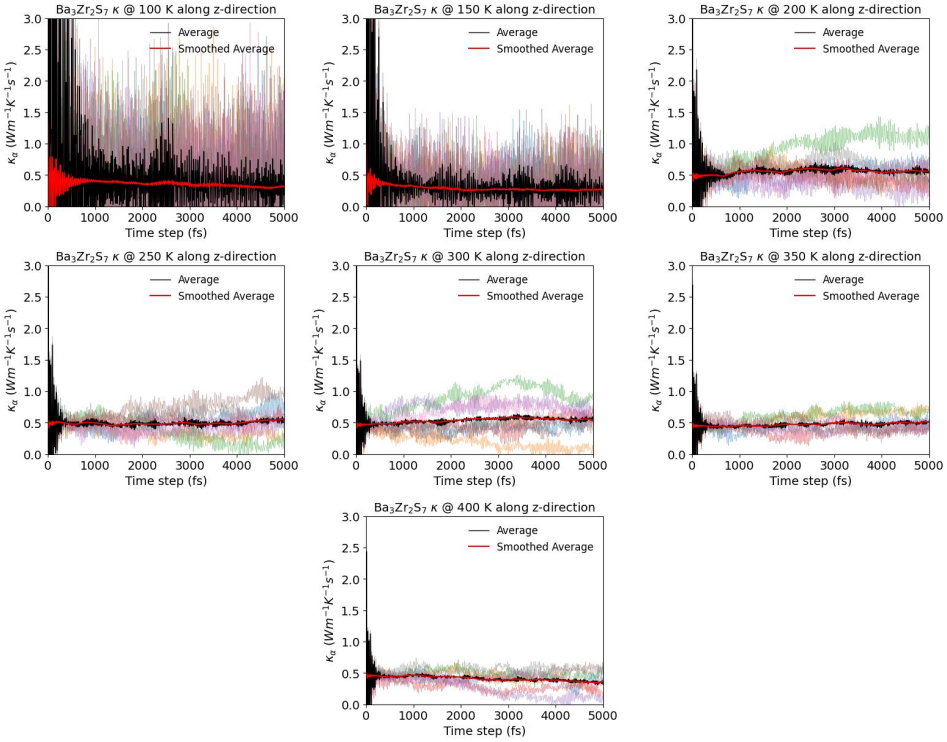

Figure S16: The calculated thermal conductivities of $Ba_3Zr_2S_7$ as a function of correlation time at various considered temperatures. Only the z-components of the thermal conductivity are plotted. Within each panel, the colorful curves represent the calculated results for all eight cases at each temperature. The black curves depict the average of the eight colorful curves, while the red curves are obtained by averaging every 200 data points from the black curve.

S22. DFT-calculated phonon dispersion

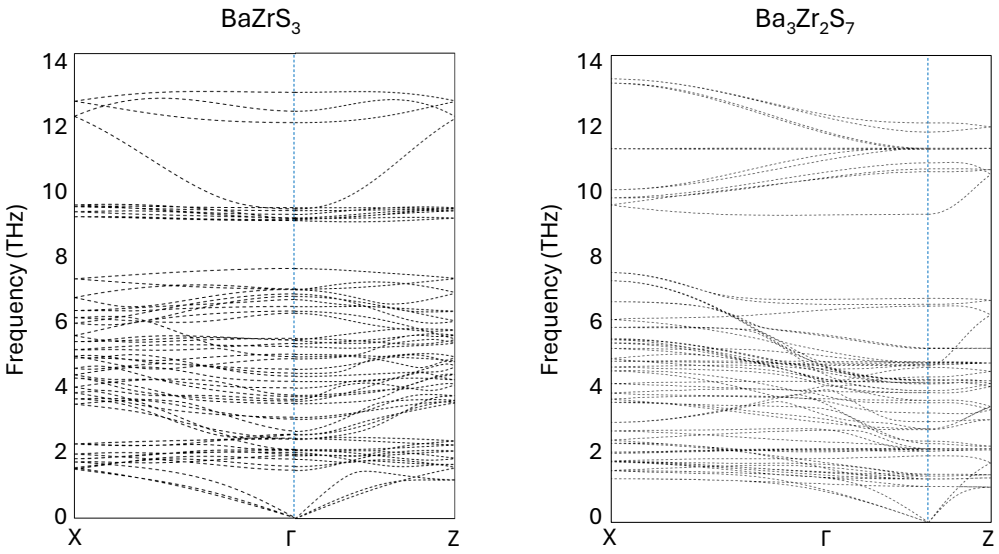

Figure S17: DFT-calculated phonon dispersion of $BaZrS_3$ and $Ba_3Zr_2S_7$. Note that they are in reasonable agreement with the SED results.

S23. Eigen-displacements of phonon modes

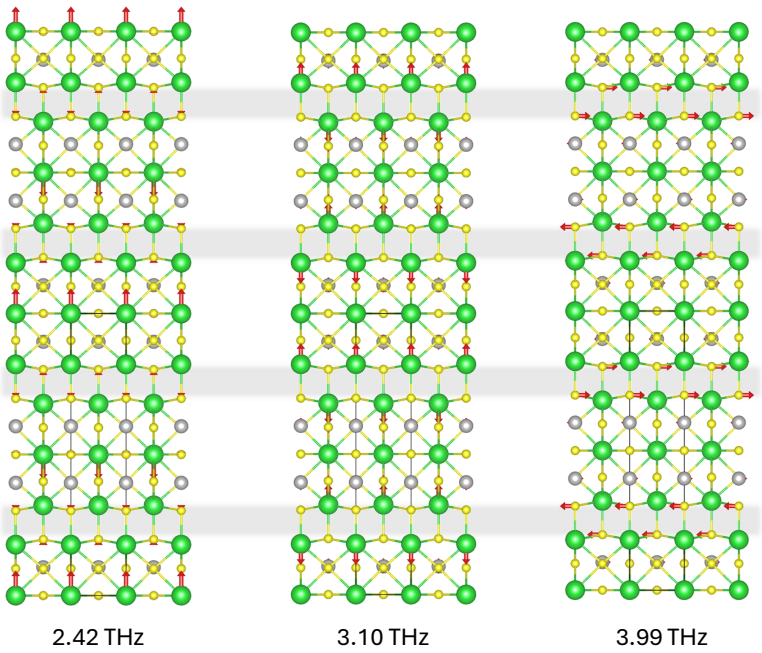

Figure S18: Eigen-displacements of three prototype phonon modes for $Ba_3Zr_2S_7$, illustrating that the inter- and intra-cell rock-salt blocks contribute to phonon localizations. The gray bars highlight the rock-salt-like interfaces.

S24. Spectral energy density of silicon

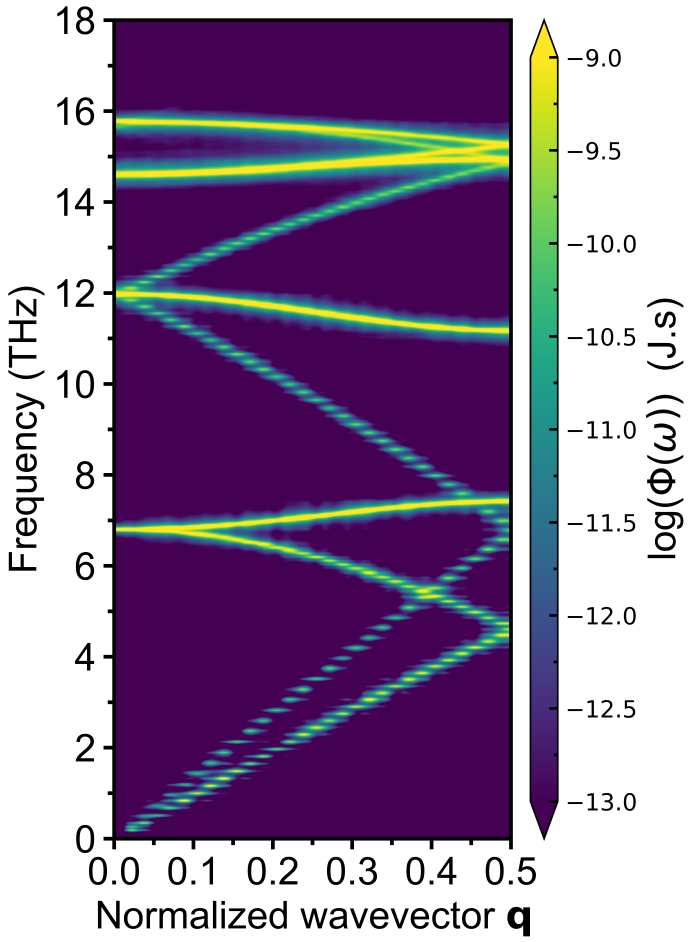

Figure S19: Calculated phonon spectral energy density for crystalline silicon at 300 K. In contrast to the chalcogenides studied in this work, the well-resolved and sharp curves show a lower degree of anharmonicity and weak coupling between the acoustic and the optical modes than in $Ba_3Zr_2S_7$.

S25. Line profiles of the valence electron densities in $BaZrS_3$ and $Ba_3Zr_2S_7$

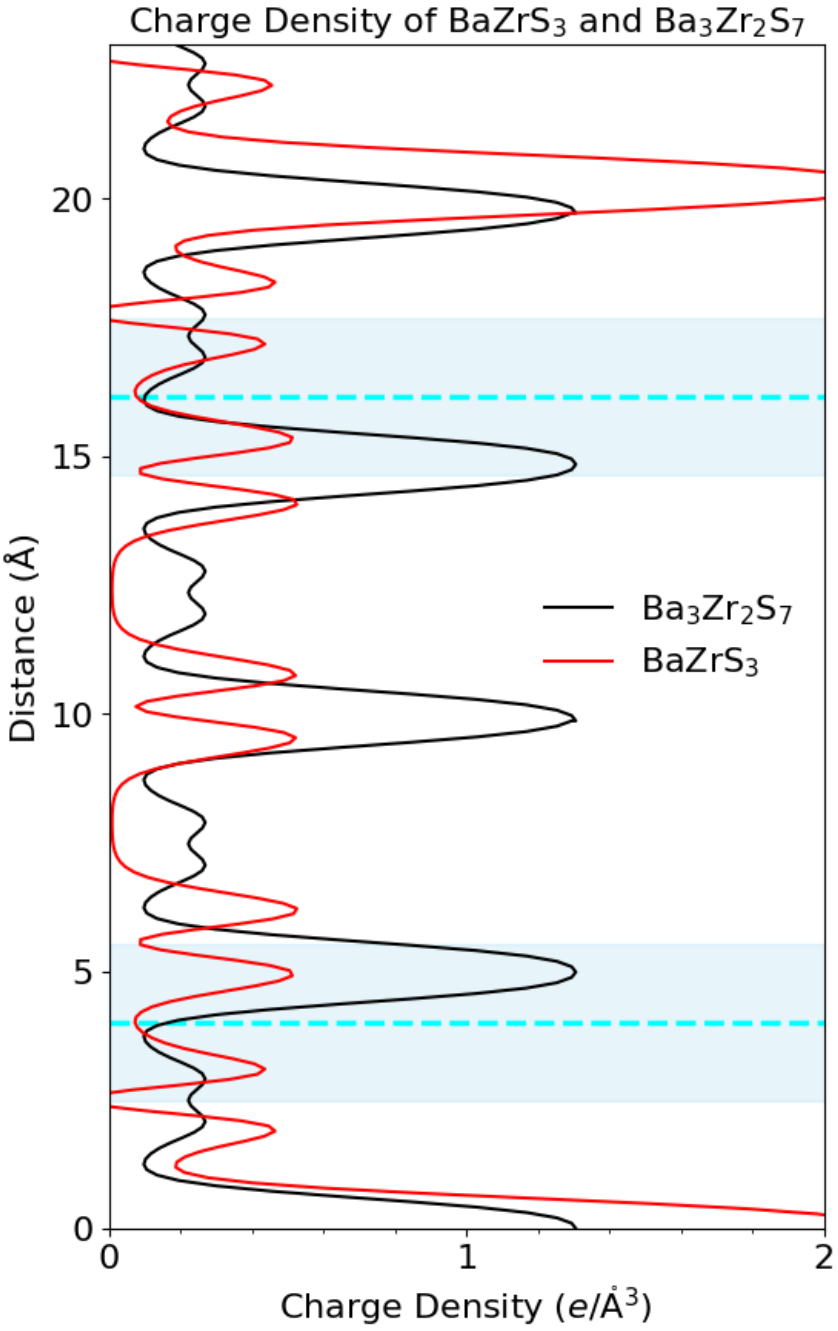

Figure S20: Line profiles of the valence electron densities along specific atomic chains in $BaZrS_3$ and $Ba_3Zr_2S_7$. The black curve is the plot in Figure 1o. The red curve represents the valence electron density through an atomic chain in $BaZrS_3$, analogous to the chain specified for $Ba_3Zr_2S_7$ in Figure 1m. The two curves are aligned by setting the zero point at the Ba atoms, which exhibit maximum values in both cases. The blue windows indicate the interface regions. The cyan dashed lines highlight the middle of the interface regions, consistent with Figures 1m and 1n. Notably, the valence electron density at the interfaces in $Ba_3Zr_2S_7$ is not only non-zero but also comparable to that between two strongly bonded atoms in the $BaZrS_3$ parent, which further demonstrates the non-vdW nature of the interfaces in $Ba_3Zr_2S_7$.

References

[1] Ye, K.; Koocher, N. Z.; Filippone, S.; Niu, S.; Zhao, B.; Yeung, M.; Bone, S.; Robinson, A. J.; Vora, P.; Schleife, A.; others Low-energy electronic structure of perovskite and Ruddlesden-Popper semiconductors in the Ba-Zr-S system probed by bond-selective polarized x-ray absorption spectroscopy, infrared reflectivity, and Raman scattering. *Physical Review B* **2022**, *105*, 195203.

[2] Niu, S.; Zhao, B.; Ye, K.; Bianco, E.; Zhou, J.; McConney, M. E.; Settens, C.; Haiges, R.; Jaramillo, R.; Ravichandran, J. Crystal growth and structural analysis of perovskite chalcogenide BaZrS3 and Ruddlesden–Popper phase Ba3Zr2S7. *Journal of Materials Research* **2019**, *34*, 3819–3826.

[3] Surendran, M.; Chen, H.; Zhao, B.; Thind, A. S.; Singh, S.; Orvis, T.; Zhao, H.; Han, J.-K.; Htoon, H.; Kawasaki, M.; others Epitaxial thin films of a chalcogenide perovskite. *Chemistry of Materials* **2021**, *33*, 7457–7464.

[4] Zhao, B.; Chen, H.; Ahsan, R.; Hou, F.; Hoglund, E. R.; Singh, S.; Shanmugasundaram, M.; Zhao, H.; Krayev, A. V.; Htoon, H.; others Photoconductive Effects in Single Crystals of BaZrS3. *ACS Photonics* **2024**, *11*, 1109–1116.

[5] Chen, H.; Singh, S.; Surendran, M.; Zhao, B.; Wang, Y.-T.; Ravichandran, J. Electrical contacts for high performance optoelectronic devices of BaZrS3 single crystals. *arXiv preprint arXiv:2409.00595* **2024**,

[6] DeCoster, M. E.; Chen, X.; Zhang, K.; Rost, C. M.; Hoglund, E. R.; Howe, J. M.; Beechem, T. E.; Baumgart, H.; Hopkins, P. E. Thermal conductivity and phonon scattering processes of ALD grown PbTe–PbSe thermoelectric thin films. *Advanced Functional Materials* **2019**, *29*, 1904073.

[7] Koh, Y. K.; Singer, S. L.; Kim, W.; Zide, J. M.; Lu, H.; Cahill, D. G.; Majumdar, A.; Gossard, A. C. Comparison of the 3 ω method and time-domain thermoreflectance for measurements of the cross-plane thermal conductivity of epitaxial semiconductors. *Journal of Applied Physics* **2009**, *105*, 054303.

[8] Jiang, P.; Huang, B.; Koh, Y. K. Accurate measurements of cross-plane thermal conductivity of thin films by dual-frequency time-domain thermoreflectance (TDTR). *Review of Scientific Instruments* **2016**, *87*, 075101.

[9] Giri, A.; Niemelä, J.-P.; Tynell, T.; Gaskins, J. T.; Donovan, B. F.; Karppinen, M.; Hopkins, P. E. Heat-transport mechanisms in molecular building blocks of inorganic/organic hybrid superlattices. *Physical Review B* **2016**, *93*, 115310.

[10] Braun, J. L.; Szwejkowski, C. J.; Giri, A.; Hopkins, P. E. On the steady-state temperature rise during laser heating of multilayer thin films in optical pump–probe techniques. *Journal of Heat Transfer* **2018**, *140*.

[11] Sun, B.; Niu, S.; Hermann, R. P.; Moon, J.; Shulumba, N.; Page, K.; Zhao, B.; Thind, A. S.; Mahalingam, K.; Milam-Guerrero, J.; others High frequency atomic tunneling yields ultralow and glass-like thermal conductivity in chalcogenide single crystals. *Nature Communications* **2020**, *11*, 6039.

[12] Braun, J. L.; Olson, D. H.; Gaskins, J. T.; Hopkins, P. E. A steady-state thermoreflectance method to measure thermal conductivity. *Review of Scientific Instruments* **2019**, *90*, 024905.

[13] Wei, C.; Zheng, X.; Cahill, D. G.; Zhao, J.-C. Invited Article: Micron resolution spatially resolved measurement of heat capacity using dual-frequency time-domain thermoreflectance. *Review of Scientific Instruments* **2013**, *84*.

[14] Yang, J.; Ziade, E.; Schmidt, A. J. Uncertainty analysis of thermoreflectance measurements. *Review of scientific instruments* **2016**, *87*.

[15] Touloukian, Y.; Boyco, E. Specific Heat: Metallic Solids volume 4 of Thermophysical Properties of Matter Eds YS Touloukian. *CY Ho (New York: IFI/Plenum)* **1970**,

[16] O'Hara, K.; Hu, X.; Cahill, D. G. Characterization of nanostructured metal films by picosecond acoustics and interferometry. *Journal of Applied Physics* **2001**, *90*, 4852–4858.

[17] Park, J.-H.; Choi, Y.-S.; Shim, H. C.; Ahn, J.-P.; Lee, J.-C. Direct Measurement of Electric Resistivity of Solid Electrolyte Interface Using 4-Point-Probe Technique. *Korean Journal of Metals and Materials* **2018**, *57*, 67–70.

[18] Koh, Y. R.; Shi, J.; Wang, B.; Hu, R.; Ahmad, H.; Kerdsongpanya, S.; Milosevic, E.; Doolittle, W. A.; Gall, D.; Tian, Z.; others Thermal boundary conductance across epitaxial metal/sapphire interfaces. *Physical Review B* **2020**, *102*, 205304.

[19] Hoque, M. S. B.; Koh, Y. R.; Braun, J. L.; Mamun, A.; Liu, Z.; Huynh, K.; Liao, M. E.; Hussain, K.; Cheng, Z.; Hoglund, E. R.; others High in-plane thermal conductivity of aluminum nitride thin films. *ACS nano* **2021**, *15*, 9588–9599.

[20] Hoque, M. S. B.; Koh, Y. R.; Aryana, K.; Hoglund, E. R.; Braun, J. L.; Olson, D. H.; Gaskins, J. T.; Ahmad, H.; Elahi, M. M. M.; Hite, J. K.; others Thermal conductivity measurements of sub-surface buried substrates by steady-state thermoreflectance. *Review of Scientific Instruments* **2021**, *92*, 064906.

[21] Kresse, G.; Joubert, D. From ultrasoft pseudopotentials to the projector augmented-wave method. *Physical review b* **1999**, *59*, 1758.

[22] Hafner, J. Ab-initio simulations of materials using VASP: Density-functional theory and beyond. *Journal of computational chemistry* **2008**, *29*, 2044–2078.

[23] Perdew, J. P.; Ruzsinszky, A.; Csonka, G. I.; Vydrov, O. A.; Scuseria, G. E.; Constantin, L. A.; Zhou, X.; Burke, K. Restoring the density-gradient expansion for exchange in solids and surfaces. *Physical review letters* **2008**, *100*, 136406.

[24] Methfessel, M.; Paxton, A. High-precision sampling for Brillouin-zone integration in metals. *Physical Review B* **1989**, *40*, 3616.

[25] Monkhorst, H. J.; Pack, J. D. Special points for Brillouin-zone integrations. *Physical review B* **1976**, *13*, 5188.

[26] Togo, A.; Tanaka, I. First principles phonon calculations in materials science. *Scripta Materialia* **2015**, *108*, 1–5.

[27] Carrete, J.; Vermeersch, B.; Katre, A.; van Roekeghem, A.; Wang, T.; Madsen, G. K.; Mingo, N. almaBTE: A solver of the space–time dependent Boltzmann transport equation for phonons in structured materials. *Computer Physics Communications* **2017**, *220*, 351–362.

[28] Li, W.; Mingo, N.; Lindsay, L.; Broido, D. A.; Stewart, D. A.; Katcho, N. A. Thermal conductivity of diamond nanowires from first principles. *Physical Review B* **2012**, *85*, 195436.

[29] Osei-Agyemang, E.; Balasubramanian, G. Understanding the extremely poor Lattice thermal transport in chalcogenide perovskite BaZrS3. *ACS Applied Energy Materials* **2019**, *3*, 1139–1144.

[30] Kresse, G.; Furthmüller, J. Efficient iterative schemes for ab initio total-energy calculations using a plane-wave basis set. *Physical review B* **1996**, *54*, 11169.

[31] Blöchl, P. E. Projector augmented-wave method. *Physical review B* **1994**, *50*, 17953.

[32] Perdew, J. P.; Zunger, A. Self-interaction correction to density-functional approximations for many-electron systems. *Physical Review B* **1981**, *23*, 5048.

[33] Novikov, I. S.; Gubaev, K.; Podryabinkin, E. V.; Shapeev, A. V. The MLIP package: moment tensor potentials with MPI and active learning. *Machine Learning: Science and Technology* **2020**, *2*, 025002.

[34] Kryuchkov, N. P.; Yurchenko, S. O.; Fomin, Y. D.; Tsiok, E. N.; Ryzhov, V. N. Complex crystalline structures in a two-dimensional core-softened system. *Soft Matter* **2018**, *14*, 2152–2162.

[35] Wang, Z.; Safarkhani, S.; Lin, G.; Ruan, X. Uncertainty quantification of thermal conductivities from equilibrium molecular dynamics simulations. *International Journal of Heat and Mass Transfer* **2017**, *112*, 267–278.

[36] Green, M. S. Markoff random processes and the statistical mechanics of time-dependent phenomena. II. Irreversible processes in fluids. *The Journal of chemical physics* **1954**, *22*, 398–413.

[37] Kubo, R. Statistical-mechanical theory of irreversible processes. I. General theory and simple applications to magnetic and conduction problems. *Journal of the physical society of Japan* **1957**, *12*, 570–586.

[38] Turney, J.; McGaughey, A.; Amon, C. Assessing the applicability of quantum corrections to classical thermal conductivity predictions. *Physical Review B* **2009**, *79*, 224305.

[39] Thomas, J. A.; Turney, J. E.; Iutzi, R. M.; Amon, C. H.; McGaughey, A. J. Predicting phonon dispersion relations and lifetimes from the spectral energy density. *Physical Review B* **2010**, *81*, 081411.

[40] Thomas, J. A.; Turney, J. E.; Iutzi, R. M.; Amon, C. H.; McGaughey, A. J. Erratum: Predicting phonon dispersion relations and lifetimes from the spectral energy density [Phys. Rev. B 81, 081411 (R)(2010)]. *Physical Review B* **2015**, *91*, 239905.

[41] Hoover, W. G. Canonical dynamics: Equilibrium phase-space distributions. *Physical review A* **1985**, *31*, 1695.

[42] Oliver, W. C.; Pharr, G. M. An improved technique for determining hardness and elastic modulus using load and displacement sensing indentation experiments. *Journal of materials research* **1992**, *7*, 1564–1583.

[43] Ding, Z.; Ridley, M.; Deijkers, J.; Liu, N.; Hoque, M. S. B.; Gaskins, J.; Zebarjadi, M.; Hopkins, P. E.; Wadley, H.; Opila, E.; others The thermal and mechanical properties of hafnium orthosilicate: experiments and first-principles calculations. *Materialia* **2020**, *12*, 100793.

[44] Braun, J. L.; Rost, C. M.; Lim, M.; Giri, A.; Olson, D. H.; Kotsonis, G. N.; Stan, G.; Brenner, D. W.; Maria, J.-P.; Hopkins, P. E. Charge-induced disorder controls the thermal conductivity of entropy-stabilized oxides. *Advanced materials* **2018**, *30*, 1805004.

[45] Zhang, P.; Chen, B.; Zhu, W.; Wang, C.; Zhang, W.; Li, Y.; Liu, W. First-principles prediction of structural, mechanical and thermal properties of perovskite BaZrS3. *The European Physical Journal B* **2020**, *93*, 1–7.

[46] Xia, Y.; Gao, Y.; Pharr, G. M.; Bei, H. Single versus successive pop-in modes in nanoindentation tests of single crystals. *Journal of Materials Research* **2016**, *31*, 2065–2075.

[47] Braun, J. L.; King, S. W.; Giri, A.; Gaskins, J. T.; Sato, M.; Fujiseki, T.; Fujiwara, H.; Hopkins, P. E. Breaking network connectivity leads to ultralow thermal conductivities in fully dense amorphous solids. *Applied Physics Letters* **2016**, *109*, 191905.

[48] Gorham, C. S.; Gaskins, J. T.; Parsons, G. N.; Losego, M. D.; Hopkins, P. E. Density dependence of the room temperature thermal conductivity of atomic layer deposition-grown amorphous alumina (Al2O3). *Applied Physics Letters* **2014**, *104*.

[49] Hoque, M. S. B.; Brummel, I. A.; Hoglund, E. R.; Dionne, C. J.; Aryana, K.; Tomko, J. A.; Gaskins, J. T.; Hirt, D.; Smith, S. W.; Beechem, T.; others Interface-independent sound speed and thermal conductivity of atomic-layer-deposition-grown amorphous AlN/Al 2 O 3 multilayers with varying oxygen composition. *Physical Review Materials* **2023**, *7*, 025401.

[50] Beekman, M.; Cahill, D. G. Inorganic crystals with glass-like and ultralow thermal conductivities. *Crystal Research and Technology* **2017**, *52*, 1700114.

[51] Cahill, D. G.; Watson, S. K.; Pohl, R. O. Lower limit to the thermal conductivity of disordered crystals. *Physical Review B* **1992**, *46*, 6131.

[52] Chiritescu, C.; Cahill, D. G.; Nguyen, N.; Johnson, D.; Bodapati, A.; Keblinski, P.; Zschack, P. Ultralow thermal conductivity in disordered, layered WSe2 crystals. *Science* **2007**, *315*, 351–353.

[53] Duda, J. C.; Hopkins, P. E.; Shen, Y.; Gupta, M. C. Exceptionally low thermal conductivities of films of the fullerene derivative PCBM. *Physical review letters* **2013**, *110*, 015902.

[54] Wang, X.; Liman, C. D.; Treat, N. D.; Chabinyc, M. L.; Cahill, D. G. Ultralow thermal conductivity of fullerene derivatives. *Physical Review B* **2013**, *88*, 075310.

[55] Aryana, K.; Stewart, D. A.; Gaskins, J. T.; Nag, J.; Read, J. C.; Olson, D. H.; Grobis, M. K.; Hopkins, P. E. Tuning network topology and vibrational mode localization to achieve ultralow thermal conductivity in amorphous chalcogenides. *Nature communications* **2021**, *12*, 1–9.

[56] Agne, M. T.; Hanus, R.; Snyder, G. J. Minimum thermal conductivity in the context of diffuson-mediated thermal transport. *Energy & Environmental Science* **2018**, *11*, 609–616.

[57] Chen, Z.; Dames, C. An anisotropic model for the minimum thermal conductivity. *Applied Physics Letters* **2015**, *107*.

[58] Ong, W.-L.; O'Brien, E. S.; Dougherty, P. S.; Paley, D. W.; Fred Higgs III, C.; McGaughey, A. J.; Malen, J. A.; Roy, X. Orientational order controls crystalline and amorphous thermal transport in superatomic crystals. *Nature materials* **2017**, *16*, 83–88.

[59] Mason, W. Properties of transducer materials. *American Institute of Physics Handbook* **1972**, 3–118.

[60] Mason, W. Acoustic properties of solids. *American Institute of physics handbook* **1972**, 3–98.

[61] Gray, D. E. American Institute of Physics (AIP). Handbook. *New York: McGraw-Hill* **1972**,

[62] Ho, C. Y.; Powell, R. W.; Liley, P. E. Thermal conductivity of the elements. *Journal of Physical and Chemical Reference Data* **1972**, *1*, 279–421.

[63] Grimsditch, M.; Zouboulis, E.; Polian, A. Elastic constants of boron nitride. *Journal of applied physics* **1994**, *76*, 832–834.

[64] Lehmann, G.; Hess, P.; Weissmantel, S.; Reisse, G.; Scheible, P.; Lunk, A. Young's modulus and density of nanocrystalline cubic boron nitride films determined by dispersion of surface acoustic waves. *Applied Physics A* **2002**, *74*, 41–45.

[65] Chen, K.; Song, B.; Ravichandran, N. K.; Zheng, Q.; Chen, X.; Lee, H.; Sun, H.; Li, S.; Udalamatta Gamage, G. A. G.; Tian, F.; others Ultrahigh thermal conductivity in isotope-enriched cubic boron nitride. *Science* **2020**, *367*, 555–559.

[66] Yonenaga, I.; Shima, T.; Sluiter, M. H. Nano-indentation hardness and elastic moduli of bulk single-crystal AlN. *Japanese journal of applied physics* **2002**, *41*, 4620.

[67] Cheng, Z.; Koh, Y. R.; Mamun, A.; Shi, J.; Bai, T.; Huynh, K.; Yates, L.; Liu, Z.; Li, R.; Lee, E.; others Experimental observation of high intrinsic thermal conductivity of AlN. *Physical Review Materials* **2020**, *4*, 044602.

[68] Nowak, R.; Pessa, M.; Suganuma, M.; Leszczynski, M.; Grzegory, I.; Porowski, S.; Yoshida, F. Elastic and plastic properties of GaN determined by nano-indentation of bulk crystal. *Applied physics letters* **1999**, *75*, 2070–2072.

[69] Shibata, H.; Waseda, Y.; Ohta, H.; Kiyomi, K.; Shimoyama, K.; Fujito, K.; Nagaoka, H.; Kagamitani, Y.; Simura, R.; Fukuda, T. High thermal conductivity of gallium nitride (GaN) crystals grown by HVPE process. *Materials Transactions* **2007**, *48*, 2782–2786.

[70] Morelli, D.; Jovovic, V.; Heremans, J. Intrinsically minimal thermal conductivity in cubic I- V- VI 2 semiconductors. *Physical review letters* **2008**, *101*, 035901.

[71] Berri, S.; Maouche, D.; Medkour, Y. Ab initio study of the structural, electronic and elastic properties of AgSbTe2, AgSbSe2, Pr3AlC, Ce3AlC, Ce3AlN, La3AlC and La3AlN compounds. *Physica B: Condensed Matter* **2012**, *407*, 3320–3327.

[72] Miller, A.; Saunders, G.; Yogurtcu, Y. Pressure dependences of the elastic constants of PbTe, SnTe and Ge0. 08Sn0. 92Te. *Journal of Physics C: Solid State Physics* **1981**, *14*, 1569.

[73] Gerlich, D. Elastic constants of single-crystal indium arsenide. *Journal of Applied Physics* **1963**, *34*, 2915–2915.

[74] Maycock, P. Thermal conductivity of silicon, germanium, III–V compounds and III–V alloys. *Solid-state electronics* **1967**, *10*, 161–168.

[75] Xiao, Y.; Chang, C.; Pei, Y.; Wu, D.; Peng, K.; Zhou, X.; Gong, S.; He, J.; Zhang, Y.; Zeng, Z.; others Origin of low thermal conductivity in SnSe. *Physical Review B* **2016**, *94*, 125203.

[76] Elbaz, G. A.; Ong, W.-L.; Doud, E. A.; Kim, P.; Paley, D. W.; Roy, X.; Malen, J. A. Phonon speed, not scattering, differentiates thermal transport in lead halide perovskites. *Nano letters* **2017**, *17*, 5734–5739.

[77] Chung, D.-H. Elastic moduli of single crystal and polycrystalline MgO. *Philosophical Magazine* **1963**, *8*, 833–841.

[78] Bell, R.; Rupprecht, G. Elastic constants of strontium titanate. *Physical Review* **1963**, *129*, 90.

[79] Yu, C.; Scullin, M. L.; Huijben, M.; Ramesh, R.; Majumdar, A. Thermal conductivity reduction in oxygen-deficient strontium titanates. *Applied physics letters* **2008**, *92*, 191911.

[80] Oh, D.-W.; Ravichandran, J.; Liang, C.-W.; Siemons, W.; Jalan, B.; Brooks, C. M.; Huijben, M.; Schlom, D. G.; Stemmer, S.; Martin, L. W.; others Thermal conductivity as a metric for the crystalline quality of SrTiO 3 epitaxial layers. *Applied physics letters* **2011**, *98*, 221904.

[81] Vassen, R.; Cao, X.; Tietz, F.; Basu, D.; Stöver, D. Zirconates as new materials for thermal barrier coatings. *Journal of the American Ceramic Society* **2000**, *83*, 2023–2028.

[82] Lewis, F.; Saunders, N. The thermal conductivity of NiO and CoO at the Neel temperature. *Journal of Physics C: Solid State Physics* **1973**, *6*, 2525.

[83] Jifang, W.; Fisher, E.; Manghnzmi, M. Elastic constants of nickel oxide. *Chinese Physics Letters* **1991**, *8*, 153.

[84] Acharyya, P.; Ghosh, T.; Pal, K.; Rana, K. S.; Dutta, M.; Swain, D.; Etter, M.; Soni, A.; Waghmare, U. V.; Biswas, K. Glassy thermal conductivity in Cs3Bi2I6Cl3 single crystal. *Nature communications* **2022**, *13*, 5053.

[85] Acharyya, P.; Ghosh, T.; Pal, K.; Kundu, K.; Singh Rana, K.; Pandey, J.; Soni, A.; Waghmare, U. V.; Biswas, K. Intrinsically ultralow thermal conductivity in Ruddlesden–Popper 2D perovskite Cs2PbI2Cl2: localized anharmonic vibrations and dynamic octahedral distortions. *Journal of the American Chemical Society* **2020**, *142*, 15595–15603.

[86] Zhang, R.; Koutsos, V.; Cheung, R. Elastic properties of suspended multilayer WSe2. *Applied Physics Letters* **2016**, *108*.

[87] Mandal, A.; Goswami, S.; Das, S.; Swain, D.; Biswas, K. New Lead-free Hybrid Layered Double Perovskite Halides: Synthesis, Structural Transition and Ultralow Thermal Conductivity. *Angewandte Chemie* **2024**, *136*, e202406616.

[88] Dawley, N. M.; Pek, E. K.; Lee, C. H.; Ragasa, E. J.; Xiong, X.; Lee, K.; Phillpot, S. R.; Chernatynskiy, A. V.; Cahill, D. G.; Schlom, D. G. Thermal Conductivity of the n= 1-5 and 10 Members of the (SrTiO3)nSrO Ruddlesden-Popper Superlattices. **2021**,

[89] Tachibana, M.; Kolodiazhnyi, T.; Takayama-Muromachi, E. Thermal conductivity of perovskite ferroelectrics. *Applied Physics Letters* **2008**, *93*, 092902.

[90] Lee, W.; Li, H.; Wong, A. B.; Zhang, D.; Lai, M.; Yu, Y.; Kong, Q.; Lin, E.; Urban, J. J.; Grossman, J. C.; others Ultralow thermal conductivity in all-inorganic halide perovskites. *Proceedings of the National Academy of Sciences* **2017**, *114*, 8693–8697.

[91] Bhui, A.; Ghosh, T.; Pal, K.; Singh Rana, K.; Kundu, K.; Soni, A.; Biswas, K. Intrinsically Low Thermal Conductivity in the n-Type Vacancy-Ordered Double Perovskite Cs2SnI6: Octahedral Rotation and Anharmonic Rattling. *Chemistry of Materials* **2022**, *34*, 3301–3310.

[92] Cahill, D. G.; Melville, A.; Schlom, D. G.; Zurbuchen, M. A. Low thermal conductivity of CsBiNb 2 O 7 epitaxial layers. *Applied Physics Letters* **2010**, *96*, 121903.